Performance study of passive acoustic systems for detecting North Atlantic right whales in seaways: the Honguedo strait in the Gulf of St. Lawrence

Cédric Gervaise, Yvan Simard, Florian Aulanier, and Nathalie Roy

Fisheries and Oceans Canada
Science Branch
Maurice Lamontagne Institute
850 route de la Mer, P.O. Box 1000
Mont-Joli, Québec
Canada G5H 3Z4

2019

Canadian Technical Report of Fisheries and Aquatic Sciences 3346

Fisheries and Oceans Canada | Pêches et Océans Canada

Canada

Canadian Technical Report of Fisheries and Aquatic Sciences

Technical reports contain scientific and technical information that contributes to existing knowledge but which is not normally appropriate for primary literature Technical reports are directed primarily toward a worldwide audience and have an international distribution. No restriction is placed on subject matter and the series reflects the broad interests and policies of Fisheries and Oceans Canada, namely, fisheries and aquatic sciences.

Technical reports may be cited as full publications. The correct citation appears above the abstract of each report. Each report is abstracted in the data base *Aquatic Sciences and Fisheries Abstracts*.

Technical reports are produced regionally but are numbered nationally. Requests for individual reports will be filled by the issuing establishment listed on the front cover and title page.

Numbers 1-456 in this series were issued as Technical Reports of the Fisheries Research Board of Canada. Numbers 457-714 were issued as Department of the Environment, Fisheries and Marine Service, Research and Development Directorate Technical Reports. Numbers 715-924 were issued as Department of Fisheries and Environment, Fisheries and Marine Service Technical Reports. The current series name was changed with report number 925.

Rapport technique canadien des sciences halieutiques et aquatiques

Les rapports techniques contiennent des renseignements scientifiques et techniques qui constituent une contribution aux connaissances actuelles, mais qui ne sont pas normalement appropriés pour la publication dans un journal scientifique. Les rapports techniques sont destinés essentiellement à un public international et ils sont distribués à cet échelon. II n'y a aucune restriction quant au sujet; de fait, la série reflète la vaste gamme des intérêts et des politiques de Pêches et Océans Canada, c'est-à-dire les sciences halieutiques et aquatiques.

Les rapports techniques peuvent être cités comme des publications à part entière Le titre exact figure au-dessus du résumé de chaque rapport. Les rapports techniques sont résumés dans la base de données *Résumés des sciences aquatiques et halieutiques*.

Les rapports techniques sont produits à l'échelon régional, mais numérotés à l'échelon national. Les demandes de rapports seront satisfaites par l'établissement auteur dont le nom figure sur la couverture et la page du titre.

Les numéros 1 à 456 de cette série ont été publiés à titre de Rapports techniques de l'Office des recherches sur les pêcheries du Canada. Les numéros 457 à 714 sont parus à titre de Rapports techniques de la Direction générale de la recherche et du développement, Service des pêches et de la mer, ministère de l'Environnement. Les numéros 715 à 924 ont été publiés à titre de Rapports techniques du Service des pêches et de la mer, ministère des Pêches et de l'Environnement. Le nom actuel de la série a été établi lors de la parution du numéro 925.

Canadian Technical Report of
Fisheries and Aquatic Sciences 3346

2019

Performance study of passive acoustic systems for detecting North Atlantic right whales in seaways: the Honguedo strait in the Gulf of St. Lawrence

by

Cédric Gervaise[1], Yvan Simard[2], Florian Aulanier[2], and Nathalie Roy[2]

[1]CHORUS research institute
Phelma Minatec
3 Parvis Louis Neel
38000 Grenoble
France

[2]Fisheries and Oceans Canada
Sciences Branch
Maurice Lamontagne Institute
850 route de la Mer, P.O. Box 1000
Mont-Joli, Québec
Canada G5H 3Z4

Cat. No. Fs 97-6/3346E-PDF ISBN 978-0-660-33170-6 ISSN 1488-5379

Correct citation for this publication:

Gervaise, C., Simard, Y., Aulanier, F., and Roy, N. 2019. Performance study of passive acoustic systems for detecting North Atlantic right whales in seaways: the Honguedo strait in the Gulf of St. Lawrence. Can. Tech. Rep. Fish. Aquat. Sci. 3346: ix + 53 p.

TABLE OF CONTENTS

Page

LIST OF TABLES

LIST OF FIGURES

ACRONYMS

ABC:	Dynamic management sectors A, B, C
AIS:	Automatic Identification System
CCBD:	Cross Correlation Based Detector
DFO:	Department of Fisheries and Oceans
DMMTS:	Dynamic Management of Maritime Traffic Speed
EBD:	Energy Based Detector
FFT:	Fast Fourier Transform
GSL:	Gulf of St. Lawrence
LFM:	Linear Frequency Modulation
NARW:	North Atlantic Right Whale
PAM:	Passive Acoustics Monitoring
Pd:	Probability of detection
Pfa:	Probability of false alarm
PG:	Processing Gain
SAG:	Surface Active Group
SL:	Source Level
SNR:	Signal to Noise Ratio
STFT:	Short-Time Fourier Transform
TFBD:	Time Frequency Based Detector
TL:	Transmission Loss

ABSTRACT

Gervaise, C., Simard, Y., Aulanier, F., and Roy, N. 2019. Performance study of passive acoustic systems for detecting North Atlantic right whales in seaways: the Honguedo strait in the Gulf of St. Lawrence. Can. Tech. Rep. Fish. Aquat. Sci. 3346: ix + 53 p.

This report addresses the problem of detecting and localizing whales located in a noisy seaway with passive acoustic monitoring (PAM) systems reporting the detections in real time. This general problem is methodologically addressed using the detection theory, and relevant formulas to assess the PAM performance are provided. The method is applied to the special case of North Atlantic right whales (NARW) in the Honguedo strait seaway of the Gulf of St. Lawrence. The relevant scales at stake in the area are first established before setting the parameters of realistic simulations fed with the actual shipping traffic, transmission loss (TL) from a regional acoustic propagation model accounting for the bathymetric and environmental structures, estimated NARW upcall source level (SL), and measured ship SLs of the local fleet. The tested scenarios include single hydrophone and hydrophone array PAM systems located either in the seaway, from buoys or gliders, or cabled to the coast. Three families of NARW upcall detectors, providing different levels of minimal signal to noise ratio (SNR) for detection, are compared for each scenario. A low false-alarm rate of 1 false detection per day is imposed and a probability of detection larger than 50% is retained as indicator of good performance. Results show that PAM systems located in the seaway have the lowest detection range and performance, because of the frequent masking of whale calls by the noise field radiated by each individual transiting ship. Moving the PAM system away from the seaway increases the detection probability, because the relative distance of the whale and the ships to the PAM increases, which favors higher occurrences of SNRs exceeding the detection threshold. Because the main noise sources (i.e. individual transiting ships) are localized in space, hydrophone arrays are showing the best performances as their directional hearing capacity with beamforming processing can greatly enhance the SNR. The most promising PAM system offering an effective solution to the detection of NARWs located in the Honguedo seaway, with reasonable and affordable efforts, appears to be the setup of two coastal-cabled hydrophone arrays, one on the Gaspesian coast and the other on the Anticosti Island.

RÉSUMÉ

Gervaise, C., Simard, Y., Aulanier, F., and Roy, N. 2019. Performance study of passive acoustic systems for detecting North Atlantic right whales in seaways: the Honguedo strait in the Gulf of St. Lawrence. Can. Tech. Rep. Fish. Aquat. Sci. 3346: ix + 53 p.

Ce rapport traite du problème de détection et localisation des baleines dans une voie de navigation bruyante au moyen d'un système d'acoustique passive (PAM) transmettant ses détections en temps réel. Cette problématique est abordée méthodiquement à l'aide de la théorie de la détection et les formules pertinentes pour estimer la performance PAM sont énoncées. La méthode est appliquée au cas particulier de la détection de baleines noires du nord Atlantique (NARW) dans la voie maritime du détroit d'Honguedo dans le Golfe du Saint-Laurent. Les dimensions pertinentes au problème dans cette région sont d'abord rappelées avant de déterminer les paramètres de simulations réalistes, nourries par le trafic observé, les pertes par transmission (TL) issues d'un modèle régional de propagation acoustique considérant la structure bathymétrique et environnementale, le niveau à la source (SL) estimé des sons de contact des NARWs ainsi que les niveaux SL mesurés des navires de la flotte locale. Les scénarios testés incluent des systèmes PAM à hydrophone unique et à réseaux d'hydrophones, localisés soit dans la voie maritime, à partir de bouées ou de planeurs, soit reliés à la côte par un câble. Trois familles de détecteurs des sons de contact de NARWs, fournissant différents niveaux minimaux de rapports signal-sur-bruit (SNR) pour la détection, sont comparés pour chaque scénario. Un faible taux de fausses détections de 1 fausse alarme par jour est imposé et une probabilité de détection supérieure à 50% est utilisée comme indicateur de bonne performance. Les résultats montrent que les systèmes PAM localisés dans la voie maritime fournissent les plus faibles portées de détection et performances, en raison du masquage fréquent des sons des baleines par les champs de bruit rayonnés individuellement par chaque navire en transit. Éloigner le système PAM de la voie maritime augmente la probabilité de détection, parce que la distance relative de la baleine et des navires par rapport au système PAM augmente, ce qui favorise une plus grande occurrence de SNRs qui excèdent le seuil de décision. Parce que les sources principales de bruit sont les navires individuels ponctuels, les réseaux d'hydrophones fournissent les meilleures performances parce que leur capacité d'écoute directionnelle avec traitement par formation de voie permet d'augmenter fortement le SNR. Le système PAM le plus prometteur, qui offre une solution efficace pour la détection de NARWs dans la voie maritime d'Honguedo, pour des efforts raisonnables et abordables, s'avère être l'implémentation de deux réseaux câblés d'hydrophones, un sur la côte gaspésienne, l'autre sur l'île d'Anticosti.

1. INTRODUCTION

1.1. NARW current context and threats in GSL

The North Atlantic right whale (*Eubalaena glacialis*) (NARW) is listed as "endangered" according to the Canadian Species at Risk Act (SARA) (DFO 2014). In 2017, the population was estimated by some models to about 411 (Pettis et al. 2018). Historically, it was mainly distributed off eastern USA coast, from Florida, in the south, up to the Canadian coast off Labrador, in the north (Cole et al. 2013, Davis et al. 2017, DFO 2014) . Individuals have been sporadically sighted in Eastern Atlantic (*Ibid.*). In the last decades, its annual distribution reflected a seasonal migration pattern between the winter breeding grounds in the south and the summer feeding grounds in the north, notably the Gulf of Maine and the Bay of Fundy (Cole et al. 2013). This pattern changed in early 2010s, when the whales deserted these traditional feeding zones (Davis et al. 2017), where their main prey declined, possibly in response to hydro-climatic changes (Grieve et al. 2017, Meyer-Gutbrod and Greene 2018, Meyer-Gutbrod et al. 2018). Further north, in southern Gulf of St. Lawrence (GSL) feeding areas , NARW observations have considerably increased in last few years (DFO 2018, Simard et al. 2019).

This latter part of Northwest Atlantic is crossed by the main shipping traffic between the Atlantic and the Great Lakes (Simard et al. 2014). The area is also the site of an intensive fixed-gear fishing activity, notably for snow crab. In 2017, the marked increase in NARW occurrence in GSL resulted in the death of 12 individuals, some of them due to collision with ships and entanglement in fishing gears (Daoust et al. 2017). No mortality in GSL were reported in 2018. In 2019, 9 mortalities were reported for June and July.

The Canadian Government has since taken action to minimize this NARW mortality, by limiting fixed-gear fishing and reducing ship speed in areas of high NARW occurrence (DFO 2019, Transport Canada 2019). This latter management measure includes a large static speed restriction zone during NARW presence season, and dynamic management sectors in the main seaways (see Figure 1, zones A, B, C, and D) where the speed restriction is triggered by the presence of a whale. This information is presently obtained from visual observations from aircrafts or boats. Such observations require adequate meteorological conditions and are limited to the daylight period. To increase the surveillance effort, real-time acoustic detection techniques based on NARW specific calls, known as PAM (Passive Acoustic Monitoring), are considered. Such techniques are presently used from fixed Ocean Observing Systems (OOS) buoys (DFO OOS Viking-WOW buoys, https://ogsl.ca/viking/) and moving platforms (Slocum glider, https://whalemap.ocean.dal.ca/WhaleMap/). The present study examines various PAM systems for real-time detection of NARW specific calls in the dynamic management sectors.

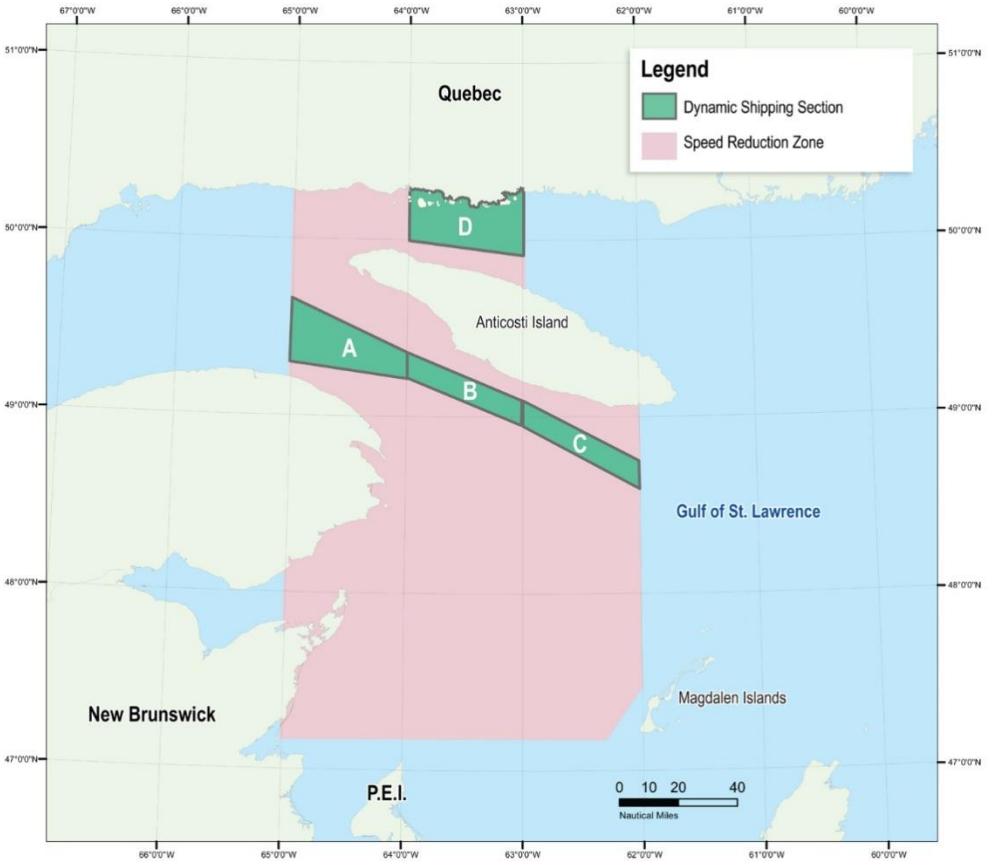

Figure 1. Map of the 10-knot static speed restriction zone for vessels longer than 20 m between April 28th and November 15th 2019 (pink) and dynamic management sectors (green, A, B, C, D) where the restriction is enforced if a NARW is detected in the last 15 days.

1.2. Objectives

In January 2019, CHORUS Research Institute (www.chorusacoustics.com) was mandated by DFO to perform a desktop study of the abilities of several PAM systems to detect and localize NARW in real-time, from their specific calls, in zones A, B, C, D of the dynamic management sectors of the maritime traffic speed in the Gulf of St. Lawrence (DMMTS). In present study, by real-time we refer to a maximum of 1-h interval after the occurrence of the event. The study was expected to rely upon a strong theoretical background and to be as realistic as possible. Its goals were to assess the detection areas and the abilities of the tested PAM systems to localize the NARW calls, and to define the *ad hoc* PAM networks required for this task.

We examined two candidate positions for the PAM networks (Figure 2). Honguedo strait position, in DMMTS sector B, was used to simulate the implementation of PAM systems on moored buoys and gliders (when several receiving depths are accounted for), within the hotspot of potential interactions between ships and NARWs. Cloridorme, a port on the northern coast of the Gaspé peninsula, was chosen as the second position because it offers: i) the possibility to deploy

a short shore-cabled PAM network for implementing advanced processing, such as real-time beamforming with hydrophone arrays, without computational, communication or power issues, and ii) it offers the advantage of taking a step back from the DMMTS to observe the interactions between the traffic and the NARWs.

At both positions, we considered two PAM systems:

i. an isotropic single hydrophone
ii. a hydrophone array offering directional hearing capability, for separating ship noise and NARW emissions, thanks to beamforming.

Each PAM system, with or without beamforming, was examined using three types of detection algorithms, presented in descending order of theoretical performances:

i. the Cross Correlation Based Detector (CCBD), based on the cross-correlation with a copy of the signal emitted by NARWs,
ii. the Time Frequency Based Detector (TFBD), based on the degree of match with a series of attributes or a stereotype of the signal emitted by NARWs,
iii. the Energy Based Detector (EBD), based on the amount of signal energy recorded in the bandwidth of NARW emissions.

These different cases (position, single hydrophone or hydrophone array, type of detector) were compared to determine their respective detection and localization performance and which of the *ad hoc* systems is the most suitable for NARW PAM in the DMMTS sectors A, B, C, D.

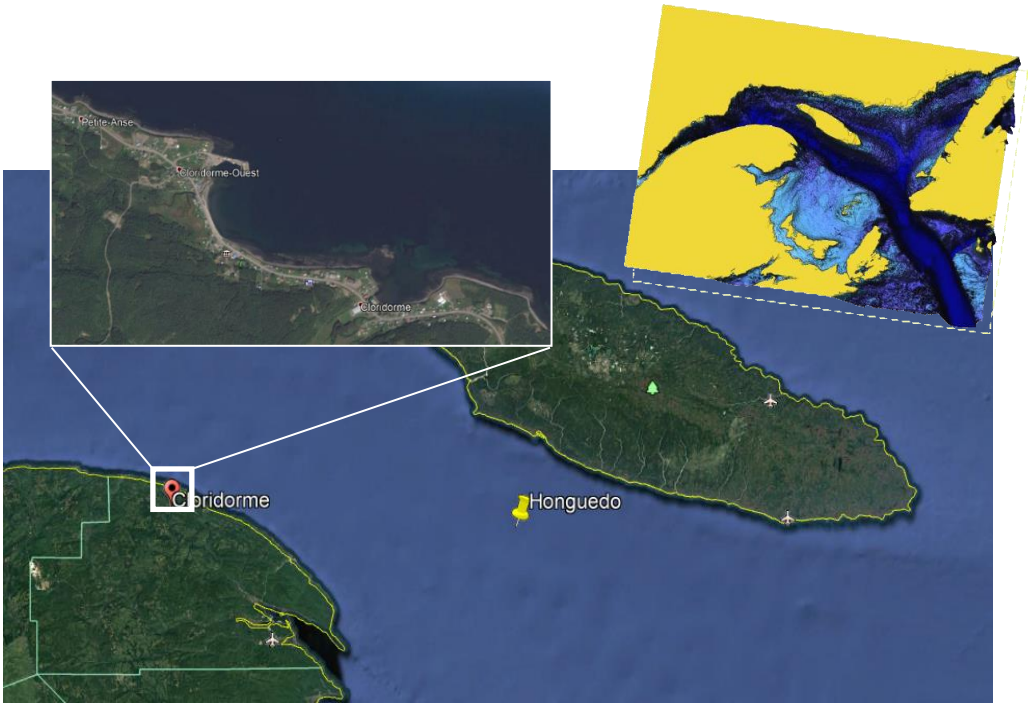

Figure 2. Positions of the two PAM systems compared for NARW detection and localization. Top right: 3D image of the GSL bathymetry, with the Laurentian Channel (dark blue).

1.3. Content of the report

Material and Methods (section 2) is divided in three parts.

Section 2.1 presents the approach used to estimate the propagation range of individual-ship noise in presence of ambient noise, and the detection range of a NARW upcall facing masking by ship noise using simplified but realistic assumptions about the spatial-temporal distribution of the shipping. It clearly demonstrates that the sounds radiated by individual ships dominate the diffused ambient noise (*sensu* NRC 2003, Wenz 1962). This discrete space-time location of the dominant ocean noise (sensu NRC 2003) source offers the opportunity to exploit beamforming filtration from a hydrophone array to enhance the signal to noise ratio (SNR) and increase the detection range.

Section 2.2 sets all the inputs and assumptions required to perform a more realistic evaluation. In section 2.2.2, we characterize NARW 'upcalls' or 'contact calls' (chirps, 1 s, ~[100 Hz-200 Hz], 165 dB re 1 µPa rms @ 1 m) as the best candidate for PAM of NARW because of their recurrence rate, their relatively large propagation range due to their low frequency and relatively loud source level (SL) and their specific time-frequency modulation allowing their recognition among calls from other species. Section 2.2.3 presents the 2017 AIS shipping traffic in dynamic management sectors A, B, C, D of DMMTS, and how we set the speed and SL of individual ships based on Simard et al. (2016). Section 2.2.4 describes the regional model and environmental data used to compute the transmission loss (TL) in a 100-km radius around the Cloridorme and Honguedo receiving positions (Aulanier et al. 2016a), and the diffuse ambient noise from Wenz (1962)'s empirical model.

Section 2.3 presents the three detectors (i.e. detection algorithms) considered to detect the NARW-upcall, in descending order of performance (CCBD, TFBD, EBD) . We derive the PAM system performance (Probability of Detection (P_d), Probability of False Alarm (P_{fa}), SNR) for each detector. To insure rigorous comparisons between the three detectors, the performances are presented considering the same SNR between the NARW upcall and the total noise. A functioning point is defined ($P_d = 0.5$, $P_{fa} = 2\times10^{-6}$ corresponding to 1 false alarm per day), and minimum SNRs to achieve this functioning point are given. The section ends with the case of a hydrophone array as PAM system (section 2.3.6). We derive the processing gain (PG) produced by the use of beamforming and the SNR expression for a NARW upcall embedded in diffuse ambient noise and discrete noise fields radiated by individual ships, with and without beamforming PG.

Section 3 (Results) compares the detection performance estimates with maps of the proportion of time where P_d is higher than 0.5 and $P_{fa} = 2\times10^{-6}$, for the different scenarios (position, single hydrophone, hydrophone array, type of detector) within 100-km radius around the receiving PAM system. These maps are obtained by simulating the 2017 dynamic shipping noise from 6169 ships that transited in zones A, B, C with 52 560 time steps of 10 min. Then we propose a formula to compute the NARW upcall detection range. The effective ranges and areas are then computed for each (position, single hydrophone, hydrophone array, detector type) and recorded in dedicated tables.

Section 4 (Discussion) compares the relative advantages and shortcomings of *ad hoc* PAM solutions for detecting and localizing NARWs swimming in the shipping dynamic management

sectors A, B, C of DMMTS using either systems mounted on buoys or gliders, located within or away from this ABC corridor, or coastal cabled systems from Cloridorme. PAM solutions allowing NARW localization are highlighted and the case of the shipping dynamic management sector D is addressed as an extension of sectors A, B, and C.

2. MATERIALS AND METHODS

2.1. Setting the orders of magnitude

The objective of this part is to set the orders of magnitude that are used in this report. We develop a simplified approach to present the ship noise propagation range (i.e. the range over which the noise radiated by a given ship exceeds the diffuse ambient noise), and the NARW upcall detection range given masking by such ship noise.

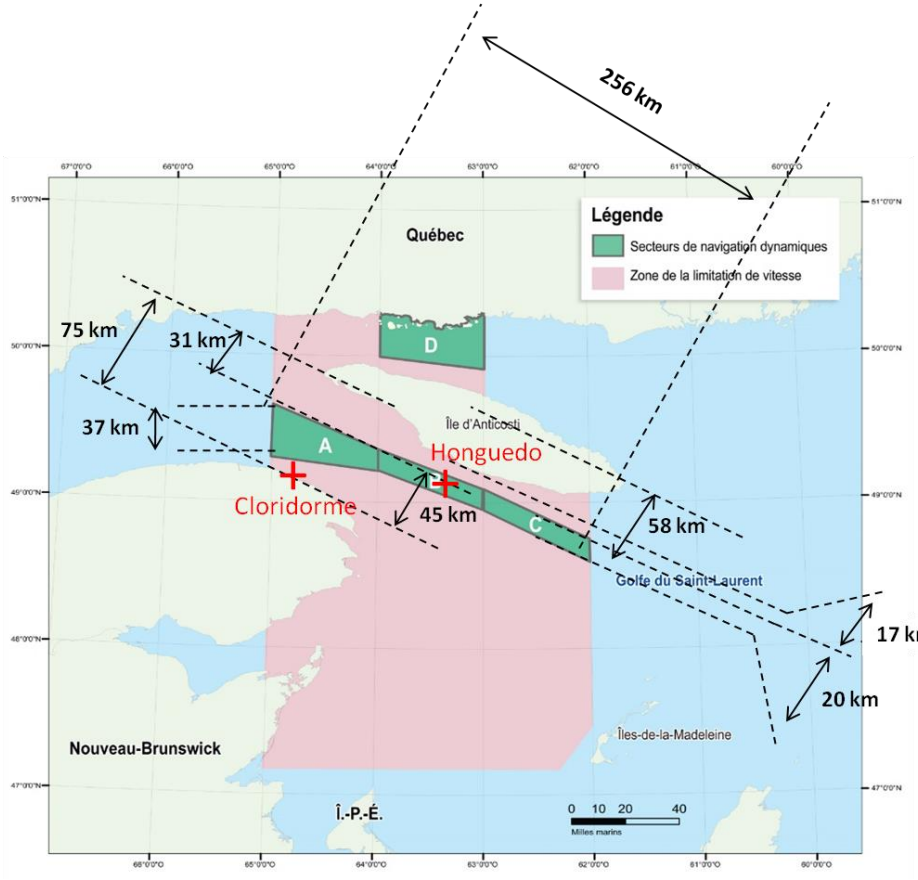

Figure 3. Map and geometry of the study area.

The geography and geometry of the area are shown in Figure 3. The sectors A, B, and C of DMMTS form a 256-m long corridor (ABC), 37-km wide at the western entrance and 20 km at the

eastern entrance. The red crosses identify the locations of the tested PAM systems at Cloridorme and in the center of the ABC dynamic management corridor in Honguedo strait.

The transverse distance between Cloridorme and the northern frontier of sector A of DMMTS is 45 km. The transverse distance between the coast of Anticosti Island[1] to the southern frontier of the zones A, B, C ranges from 37 km to 80 km.

At a speed of 14 knots (Simard et al. 2016), a ship crosses the ABC corridor in 10.15 hours. The AIS data in Table 1 indicates that 16 ships cross this ABC corridor every day on average. The cumulative ship presence in the corridor is 162.4 hours (10.15 x 16) per day which means that, on average, 7 ships (162.4/24) are present at the same time in the corridor. Under the simplified assumption that ships are uniformly distributed along the corridor, the distance between 2 consecutive ships is 36 km (256 km / 7).

To assess the single-ship noise propagation range in diffuse ambient noise (*sensu* Wenz, (1962)) and the NARW upcall propagation range, we make the following assumptions:

- Main bandwidth of NARW upcalls (see Parks et al. 2011) [100 Hz, 200 Hz]
- Typical wideband SL of a ship (Simard et al. 2016) 185 dB re 1µPa @ 1m
- Typical narrow band ship SL at 150 Hz (Simard et al. 2016) 165 dB re 1µPa^2/Hz @1m
- Typical wideband SL of a NARW upcall (Clark et al. 2011) 165 dB re 1µPa @ 1m
- Typical diffuse wideband [100, 200]Hz low noise level (Wenz 1962) 68 dB re 1µPa
- Typical diffuse narrow band low noise level (Wenz 1962) 48 dB re 1µPa
- Transmission Loss model $20\log_{10}(r)$
- SNR (P_d = 0.5, 1 false alarm/day, TFBD) 16 dB

Under these assumptions,

- at 10 dB SNR condition, the noise radiated by a ship exceeds the diffuse wideband Wenz noise up to a range of 224 km ($10^{\frac{185-68-10}{20}}/1000$),
- at 10 dB SNR condition, the NARW upcall can exceed diffuse narrow band Wenz noise up to a range of 224 km ($10^{\frac{165-48-10}{20}}/1000$).

When an individual ship is present at a distance R_s from the PAM system, it becomes the main noise contributor within a radius of 224 km and the NARW detection range, R_w, follows the relation $R_w = 1/20 \times R_s$ (see section 2.3.5 for details)[2].

These simplified computations demonstrate that, in the zones A, B, C, D of DMMTS,

- NARW upcall detection range compares to the ABC-corridor length under low diffuse noise condition,

---

[1] Considered as another candidate site for the installation of a cabled PAM system

[2] $SL_w + 10log_{10}(L_{fft}) - 20log_{10}(R_w) - (SL_s - 10log_{10}(B_w) - 20log_{10}(R_s)) = 16$

- the major noise source limiting NARW upcall detection originates more from several punctual and individual ships than from diffuse ambient noise,
- the shipping noise drastically reduces the NARW upcalls detection range, which is highly dependent on the specific arrangement of ships in the corridor at a given time t,
- as the sources of noise are punctual ships, the use of a hydrophone array to perform a directional hearing should be considered.

2.2. Acoustic and environmental inputs

2.2.1. Objectives

In this section we set all the inputs and assumptions required for realistic NARW upcall detection performance estimates using numerical simulation modeling. First, we describe the NARW upcalls. Then, we document the shipping traffic in areas A, B, C, D of DMMTS through 2017 statistics of AIS data collected by DFO. We indicate how we set the speed and SLs of individual ships using Simard et al. (2016)'s St. Lawrence fleet model. We end this part by presenting the PAM performance simulation method with the oceano-geo-acoustics parameters used to compute the transmission loss (TL) in a disc of 200 km in diameter around Cloridorme and Honguedo (Aulanier et al. 2016a, Aulanier et al. 2016b) and the diffuse ambient noise from the empirical model of Wenz (1962).

2.2.2. NARW acoustics

NARW sonic production has been described by comparison with other similar species (South Pacific right whales, North Pacific right whales) and from NARW previous and extensive studies since 2000 in their summering habitats of the north-eastern coasts of USA (Cape Code, Stellwagen Bank, Gulf of Maine) and Canada (Scotian shelf, Bay of Fundy) including recently the Gulf of St. Lawrence.

NARW calls fall into three categories presenting quite different features:

- The upcall, a stereotyped emission used to maintain contact between individuals (Clark 1982) over several miles. The upcall is a 1-s long increasing frequency modulation between 100 Hz and 200 Hz where these parameters are affected by natural variability (Clark 1982, Matthews et al. 2001, Mussoline et al. 2012, Parks et al. 2011, Simard et al. 2019) (Figure 4).
- The gunshot, a stereotyped emission appearing as a short and loud impulse extending from very low frequency (50 Hz) to mid frequency (4 kHz). The gunshot has been documented to be emitted within Surface Active Groups (SAGs), when several individuals cluster for socializing, and for reproductive advertisement (Parks et al. 2012, Parks and Tyack 2005).
- Sonic emissions during SAGs, are more frequent and more diverse (tonal, moans, impulses…). As the communication range is short in a SAG, the SL of some sounds may be weaker than the gunshot and the upcall (Parks et al. 2011, Parks and Tyack 2005, Trygonis et al. 2013).

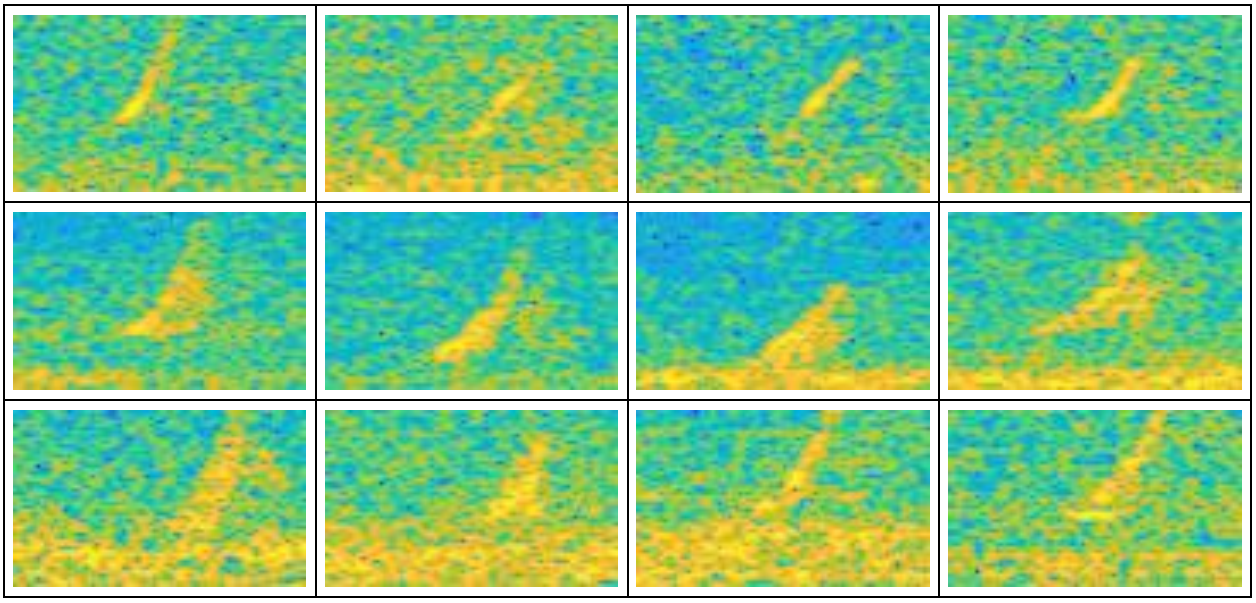

Figure 4. Spectrogram examples of NARW upcalls recorded in southern GSL in 2018. Y axis: frequency from 100 to 200 Hz; X axis: time 3 s. Resolution 3.9 Hz × 32 ms.

Although all NARW calls may be useful for monitoring purposes, the upcalls are the best candidates because they are stereotyped and can be used to identify the species. They are emitted regularly at a variable but significant rate, and their low frequency coupled with the frequency modulation ensures a long range propagation and detection (Clark et al. 2010). Upcalls were proposed and used by Mellinger et al. (2007), Clark et al. (2010), and Baumgartner et al. (2013) for NARW PAM (including from glider platforms) on the north-eastern coast of USA. Upcall detection ranges were reported to be around 10 km within an urbanized area (Clark et al. 2010) and more than 50 km for North Pacific right whales within the more pristine environment of Bering Sea (Munger et al. 2011, Wiggins et al. 2004).

NARW upcall features used in this report are coming from (Clark et al. 2011, Parks and Tyack 2005):

- Upsweep frequency modulation,
- Duration: 1 s
- Main frequency band: [100 Hz, 200 Hz],
- SL (dB re 1µPa@1m): 165 ± 3 dB re 1µPa @ 1m.

The SL from Clark et al. (2011) is conservative[1] since Munger et al. (2011) report SL ranging within 177 ±1 dB re 1 µPa @ 1 m for North Pacific right whales.

[1] In the sense of minimizing the range of detection

2.2.3. Marine traffic within the dynamic management zones

AIS messages from the ships transiting within the dynamic management zones A, B, C, and D in 2017 were collected by DFO (cf. Simard et al. 2014). They are reported on a daily basis in Table 1 and Table 2. The traffic density in ABC corridor was 16± 3 ships per day. The traffic was weakly modulated by the season, with 12 ± 4 ships per day in the first quarter compared to 17± 2 ships per day for the other 3 quarters. The traffic in corridor D averaged 2 ships per day, which is about 14% of the traffic in ABC corridor (Table 2).

Table 1. AIS traffic density (vessel per time period) in dynamic management sectors A, B, C in 2017.

Day	Jan.	Feb.	March	Apr.	May	June	July	Aug.	Sept.	Oct.	Nov.	Dec.	Year
1	22	18	15	20	18	17	21	17	11	18	13	19	
2	15	12	9	17	19	22	17	14	14	16	15	22	
3	10	10	13	14	17	21	20	15	13	21	21	20	
4	6	9	12	9	17	13	30	20	15	21	21	20	
5	12	11	9	16	14	21	25	23	14	16	21	12	
6	15	15	8	12	16	20	22	23	16	14	27	14	
7	19	4	14	9	18	24	25	15	23	20	11	18	
8	16	7	19	19	11	18	24	12	11	21	19	10	
9	13	8	16	17	18	17	24	15	16	22	21	14	
10	12	16	11	23	20	20	27	21	17	14	18	16	
11	10	11	8	28	21	30	22	16	18	11	8	14	
12	12	19	5	17	28	19	20	14	16	20	17	13	
13	7	11	10	12	30	17	15	19	17	19	31	7	
14	7	6	14	14	28	22	23	17	13	18	24	8	
15	12	10	13	23	20	23	15	17	14	24	18	9	
16	7	12	13	22	16	19	25	10	14	19	21	15	
17	13	8	12	18	10	22	25	16	17	16	21	18	
18	7	13	12	20	17	20	14	21	18	14	19	16	
19	17	19	15	15	15	17	20	16	12	17	19	13	
20	15	12	21	14	21	16	13	13	17	21	21	18	
21	19	17	10	15	21	16	11	20	19	22	17	11	
22	18	14	10	18	22	12	15	13	18	25	16	17	
23	10	12	10	17	18	24	20	14	14	21	13	12	
24	12	11	10	5	16	21	21	20	17	18	17	10	
25	8	7	8	12	21	25	20	22	21	13	24	16	
26	13	20	11	24	22	17	12	20	20	21	26	13	
27	9	11	16	19	25	15	13	16	25	11	16	8	
28	15	13	17	14	29	22	20	12	17	15	19	10	
29	15		11	19	24	18	19	22	14	17	19	15	
30	12		10	16	16	16	16	17	20	10	19	8	
31	17		12		12		17	19		14		18	
Total	**395**	**336**	**374**	**498**	**600**	**584**	**611**	**529**	**491**	**549**	**572**	**434**	**5973**
Mean	**13**	**12**	**12**	**17**	**19**	**19**	**20**	**17**	**16**	**18**	**19**	**14**	**16.4**

Table 2. AIS traffic density (vessel per time period) in dynamic management sector D in 2017.

Day	Jan.	Feb.	March	Apr.	May	June	July	Aug.	Sept.	Oct.	Nov.	Dec.	Year
1	1	2	0	0	1	2	2	0	2	6	6	5	
2	1	0	0	0	1	2	1	1	3	2	4	4	
3	1	0	0	0	1	0	4	3	7	6	4	4	
4	1	0	0	0	2	0	2	2	5	6	4	3	
5	1	1	1	1	1	1	1	1	6	6	5	4	
6	0	0	0	0	0	1	0	5	3	2	4	2	
7	1	0	0	0	0	2	3	3	4	2	3	3	
8	0	0	0	0	1	2	4	6	0	7	7	2	
9	0	0	0	1	0	0	1	5	4	10	1	3	
10	1	0	0	1	1	0	3	5	9	4	1	5	
11	3	0	0	2	1	0	3	1	4	5	0	7	
12	0	1	1	1	1	1	1	1	3	6	5	4	
13	0	2	0	0	0	1	2	6	6	4	4	2	
14	2	1	0	1	1	0	2	6	5	5	6	3	
15	2	0	0	0	1	4	1	6	7	5	4	2	
16	1	1	0	0	1	2	1	7	6	3	4	1	
17	1	0	0	0	1	0	1	3	6	4	3	5	
18	1	0	0	0	0	0	2	2	4	5	7	5	
19	0	1	0	0	0	3	6	4	4	0	6	4	
20	1	2	0	1	1	6	2	7	9	0	4	3	
21	0	0	0	0	0	3	1	5	2	4	3	3	
22	2	0	0	1	1	0	0	7	4	10	4	3	
23	0	0	1	1	1	1	1	7	7	2	7	0	
24	0	0	0	0	1	1	0	4	9	5	3	2	
25	1	0	1	1	0	4	2	4	1	8	4	1	
26	0	0	2	0	3	4	5	8	6	4	4	3	
27	0	2	0	0	4	3	4	6	4	3	3	1	
28	0	0	0	2	1	4	3	5	9	5	4	0	
29	1		0	1	2	4	1	3	6	6	4	3	
30	1		1	0	0	2	5	4	5	6	6	1	
31	1		0		1		4	2		9		0	
Total	**24**	**13**	**7**	**14**	**29**	**53**	**68**	**129**	**150**	**150**	**124**	**88**	**849**
Mean	**0.8**	**0.5**	**0.2**	**0.5**	**0.9**	**1.8**	**2.2**	**4.2**	**5.0**	**4.8**	**4.1**	**2.8**	**2.3**

2.2.4. Simulation of acoustic propagation and ambient noise within the study area

TL were computed using a 2.5-D model (i.e. 3D TL field reconstruction from the concatenation of vertical slices between sources and receivers) implemented by DFO for the St. Lawrence and Canadian Arctic (Aulanier et al. 2016a, Aulanier et al. 2017). The propagation was simulated between the sources (ship location or hypothetical whales) and receivers (candidate hydrophones or hypothetical whales) the classical RAM code (http://oalib.hlsresearch.com/PE/RAM/) (Collins 1993), a 2D parabolic equation (PE) model, fed with the high-resolution bathymetry from the DFO Canadian Hydrographic Service, range-dependent environmental conditions from several DFO operational models and published data (Loring and Nota 1973, Senneville and Lefaivre 2015).

To get NARW upcall detection probability, TL maps were computed for a 1-km × 1-km grid of potential sources within a disc of 200 km in diameter around the PAM system at 3 frequencies (100 Hz, 150 Hz, and 200 Hz). The receiver depth was set to 30 m for Cloridorme whereas 16 receiver depths (20 m to 360 m by step of 20 m) were considered for Honguedo. The NARW call depth was set to 15 m based on the observations of the upper water column calling from NARWs tracked with D-tags (Parks et al. 2011). Ship source depths were set to 4 m.

Sound speed profiles over the water column and the geo-acoustic parameters of the seafloor were derived using the data and methodology described in Aulanier et al. (2016a, p. 3).

The diffuse ambient noise level was set to 69 dB re 1 $\mu Pa^2/Hz$ at 150 Hz, corresponding to a mid-traffic condition of Wenz's empirical model (Wenz 1962).

2.3. Performances of three NARW upcall detectors from single-hydrophone or hydrophone-array setups

2.3.1. Objectives

This section presents the theoretical background for detection of NARW upcalls embedded in ship noise. The NARW upcall detection problem is presented and three detector types (CCBD, TFBD, and EBD) are examined. Performance analysis is made for each detector type using the three following criteria: Probability of Detection (P_d), Probability of False Alarm (P_{fa}), and Signal to Noise ratio (SNR). For rigorous comparisons between the detector types, the performances are presented with a unified and consistent theoretical framework, based on the same expression of SNR. The minimum SNRs to achieve a functioning point defined as ($P_d = 0.5$, $P_{fa} = 2\times10^{-6}$, corresponding to 1 false alarm per day, which can be eliminated by a human supervisor) are given for the three detectors. The section ends with the case of PAM systems using hydrophone arrays. We derive the processing gain (PG) produced by using beamforming techniques and we present the SNR required for detecting a NARW upcall embedded in diffuse ambient noise and individual ships, with or without using beamforming.

2.3.2. The data and detection problem

Let us consider an operational PAM sensor recording under noise-only conditions when a NARW upcall is absent (see Figure 5). In the specific context of the ABC dynamic management corridor and according to the conclusions of section 2.1, the noise is the sum of the emissions of several individual ships with a diffuse ambient noise *sensu* Wenz (1962). This 'noise only' case is referred to as hypothesis H_0. If a NARW upcall is present, the acoustic measurement is the sum of this upcall and the sum of the radiated noise from the ships and the diffuse ambient noise. This 'upcall-present' case is referred to as hypothesis H_1:

- Hypothesis H_0: $m(t) = \sum_{N_s} s(i,t) + b(t) = b_{tot}(t)$
- Hypothesis H_1: $m(t) = uc(t) + \sum_{N_s} s(i,t) + b(t)$

where N_s stands for the number of ships present at the same time in the corridor, s(i,t) is the noise produced by ship of index i, b(t) is the diffuse ambient noise *sensu* Wenz (1962), $b_{tot}(t)$ is the total noise and uc(t) is the upcall. b(t) and s(i,t) are supposed to be random and normally distributed (0 mean, variance σ^2), whereas uc(t) is a deterministic signal:

$$uc(t) = 0 \; if \; t \notin [0,T], uc(t) = A\cos(2\pi f_{min} t + 2\pi \frac{f_{max} - f_{min}}{2T} t^2)$$

Noise level (σ^2) and upcall level ($A/\sqrt{2}$) are given in section 2.1 for a realistic configuration.

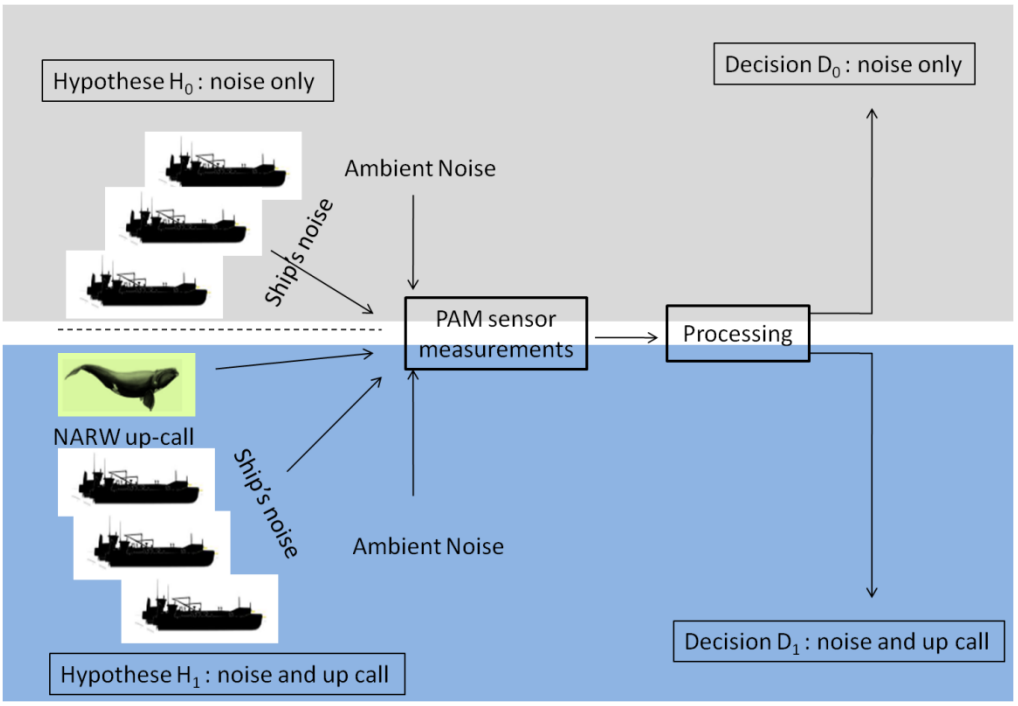

Figure 5. Environmental configuration of the detection of NARW upcalls embedded in ship noise

The detection problem is to decide if the upcall is present or absent based on the acoustic measurements m(t). Any detector follows the same 2-step logic: i) the measurements are processed to derive the probability of the selected hypothesis, i.e. the result of a statistical test T, and ii) T is compared to a threshold λ that fixes the accepted probability of false alarm (see Figure 6). If T is higher than λ, we decide that the upcall is present in the measurements and this decision is referred to as D_1; if T is lower than λ, we decide that the upcall is absent from the measurements and this decision is referred to as D_0.

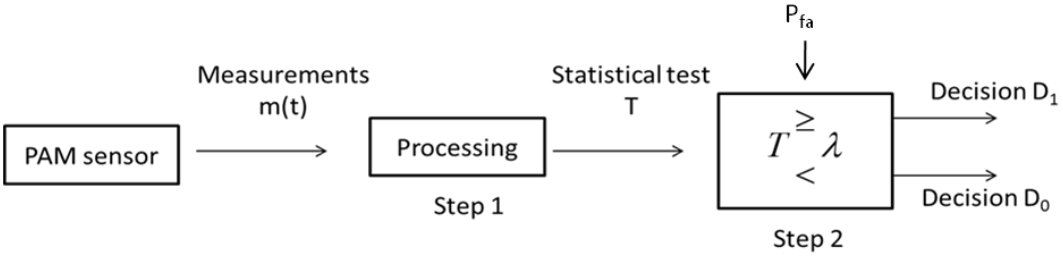

Figure 6. The two-step logic of the detection task.

Depending on the initial hypotheses H_0 and H_1, the decisions D_0 or D_1 may be right or false. Table 3 sets the vocabulary.

Table 3. The four cases of the detection problem.

		Decision	
Hypothesis		D_0	D_1
	H_0	right decision of absence Probability $1-P_{fa}$	wrong decision, false alarm Probability P_{fa}
	H_1	wrong decision, missed detection Probability $1-P_d$	right decision of presence Probability P_d

Since a false alarm of NARW upcall presence within the dynamic management sectors will trigger the speed restriction measure, we will promote detectors that ensure a constant false alarm rate, and for this family of detectors, we will look for the ones maximizing the detection probability to optimize the protection of NARWs against the risk of adverse effects of shipping (Kay 1998).

2.3.3. Choice of three NARW upcall detectors

A large range of solutions exists to detect short transient sound embedded in noise. The choice of the ideal solution is a huge task and results from a tradeoff between:

- the raw performances of detection (the best probability of detection for a given false alarm probability),
- the robustness versus the variability of the real data and the assumption used to derive the best detector (in the sense of optimizing the probability of detection),
- the computational load and the ability to run in real-time.

The scope of the present report is not to cover the whole range of solutions and to study in detail each solution but to identify the family of solutions (e.g. spectrogram based detectors, wavelet based detector, correlation with a template based detectors, etc.) that is suitable to the context of the detection of NARW upcalls in eastern Canadian waters.

First, we choose to bound the performances of detection by an upper and a lower limit. To do so, we rely upon Kay (1998):

- When we do not assume any a priori knowledge about the waveform of the upcall except its bandwidth, the detector is based on the energy of the measurements contained within the bandwidth of the upcall (Kay 1998, p. 250), this Energy Based Detector (EBD) is simple, compatible with real-time processing, and robust, but it sets the lowest bound of the detection performances,
- When we assume to know the exact waveform of the received upcall, the detector is based on the cross-correlation of the measurements with the exact copy of the received upcall (Kay 1998, p. 101). This Cross Correlation Based Detector (CCBD) sets the highest bound of the detection performances but lacks robustness versus a deviation between the template used to compute the cross-correlation and the true upcall emitted by the NARW and requires a large computational payload that can impair real-time abilities.

A bibliographic survey of solutions related by the scientific communities indicates efficient real-time solutions for NARW upcalls within Western North Atlantic waters based on the processing of the spectrogram of the measurement (Baumgartner and Mussoline 2011, Gillespie 2004, Simard et al. 2019, Urazghildiiev and Clark 2007). These four solutions fall within the family of Time Frequency Based Detectors (TFBD). Lampert and O'Keefe (2010) rewieved more than 32 declinations of TFBD applied to the passive detection of cetacean sounds. Among these numerous algorithms, Urazghildiiev et al. (2009) demonstrates that the performances of TFBD using the expected time-frequency support of the upcall as *a priori* information tend towards that of CCBDs for low SNR conditions. For these reasons, we select as a third detector, a TFBD using the expected time-frequency support of the upcall. We expect (and we will demonstrate) that this TFBD sets an optimal tradeoff between performance, robustness, and computational payload.

2.3.4. Description of the three NARW upcall detectors

Here, we describe the three NARW upcall detectors in decreasing order of performance. Figure 7 illustrates the detection steps for each of them.

CCBD, the first detector, is referred to as CCBD, for Cross Correlation Based Detector. Under certain conditions (see Kay (1998), p. 101), CCBD is optimal in the sense that it maximizes the detection probability for a given probability of false alarm. CCBD requires to know the emitted waveform of the upcall and the eventual distortion due to acoustic propagation effects. Let ref(t) be this reference; then,

- step 1 calculates the cross-correlation of the measurement with the reference, and
- step 2 tests if the value of this cross-correlation exceeds the detection threshold for the presence of the upcall.

TFBD, the second detector, is referred to as TFBD for Time Frequency Based Detector. At this step in the report, nothing is known about its optimality. What is known is that: 1) according

to Urazghildiiev et al. (2009), performances of TFBDs tend towards those of CCBDs for low SNR conditions, and 2) various TFBDs are operationally used (Baumgartner et al. 2013, Simard et al. 2019, Urazghildiiev et al. 2009). TFBD requires a time-frequency template or the attributes of the emitted upcall. Figure 7 and Figure 8 illustrate the TFBD process and its application on real data using the comparison with a time-frequency stereotype:

- step 1.1: the spectrogram of the data is computed with an adequate FFT window length (see annex 1 for the optimal FFT window length for a LFM signal such as NARW upcall).
- step 1.2: the spectrogram of the data is binarized for each time-frequency bin following the method proposed in (Dadouchi et al. 2013).
- step 1.3: the time-frequency template of the upcall (see arrow a1, plot C, Figure 8) is run over the binarized spectrogram and, for each time step, the number of time-frequency bins overlapping with the time-frequency template are counted.
- step 2: this matching sum or the proportion of match is tested against a threshold to detect or not detect the presence of an upcall.

EBD, the third detector, is referred as EBD for Energy Based Detector. EBD only requires knowing the bandwidth of the upcall. With only this limited *a priori* information, the EBD sets a worst bound of detection performance. Figure 7 illustrates the EBD process:

- step 1.1: acoustic data are band-pass filtered for the upcall bandwidth,
- step 1.2: the energy of the data is computed for a period equal to the upcall duration,
- step 2: the energy is tested against a threshold to detect the presence of an upcall.

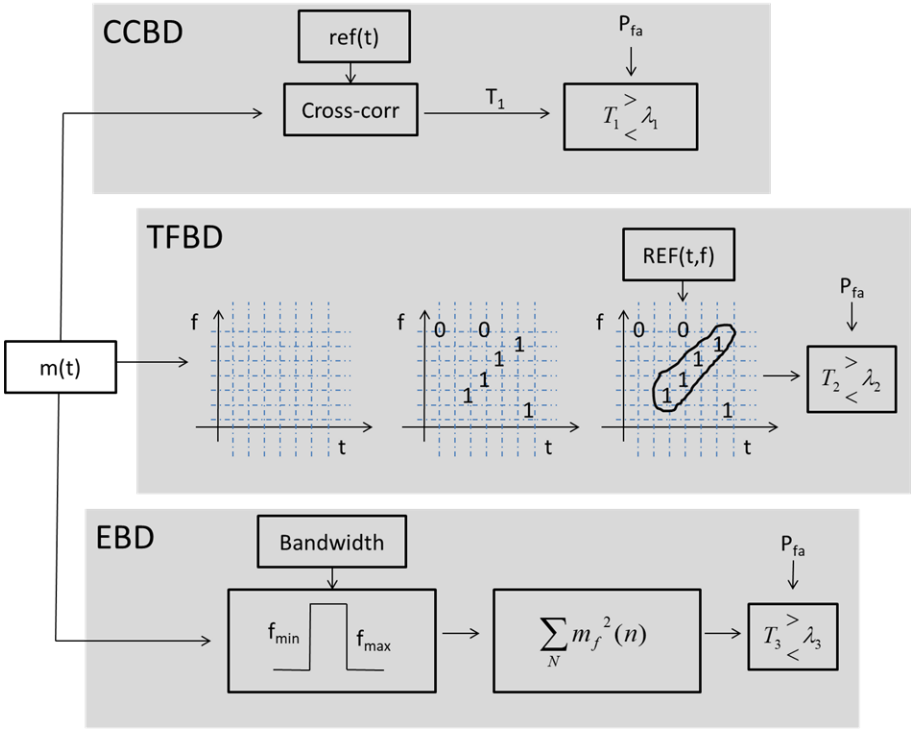

Figure 7. Schemes of the three detectors.

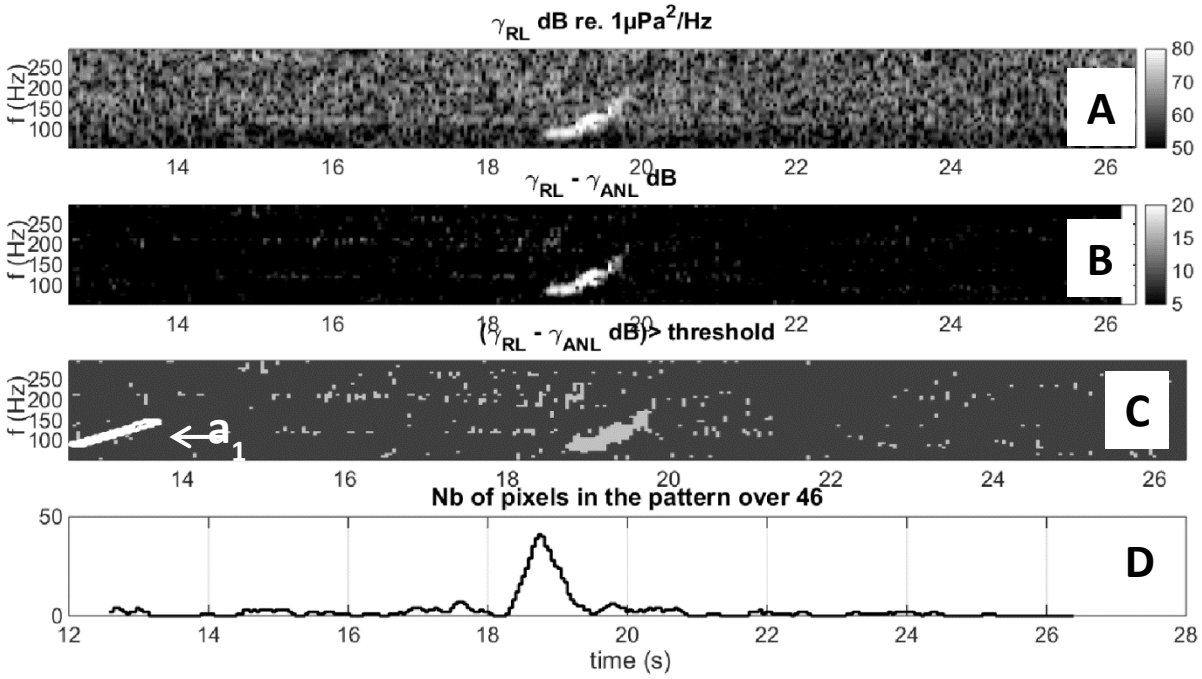

Figure 8. Step by step processing of the data for TFBD.

A: Computation of the spectrogram, B: Binarization of the spectrogram, C & D: Estimation of the proportion of match with the time-frequency template of the upcall. Application to real data collected in the Gaspé area (Gaspé B8A80989, Simard et al. 2019).

A qualitative assessment of the functioning and performance of the three detectors is presented in Figure 9, showing how each detector improves the SNR. A negative SNR (-5 dB) synthetic data snapshot was created and used for CCBD, TFBD, and EBD tests. The outputs of step 2 for each detector are plotted and we quantify their differences under noise-only and upcall-present conditions. The higher is this difference, the better is the detection performance. The EBD shows a very low change (1.7/1.4 = 1.2) whereas the CCBD change is large (5500/500 = 11). The TFBD shows an intermediate change of 48/8 = 6. This level of change is mainly created by the computation of the spectrogram magnifying the presence of the upcall (see arrow c_2, Figure 9).

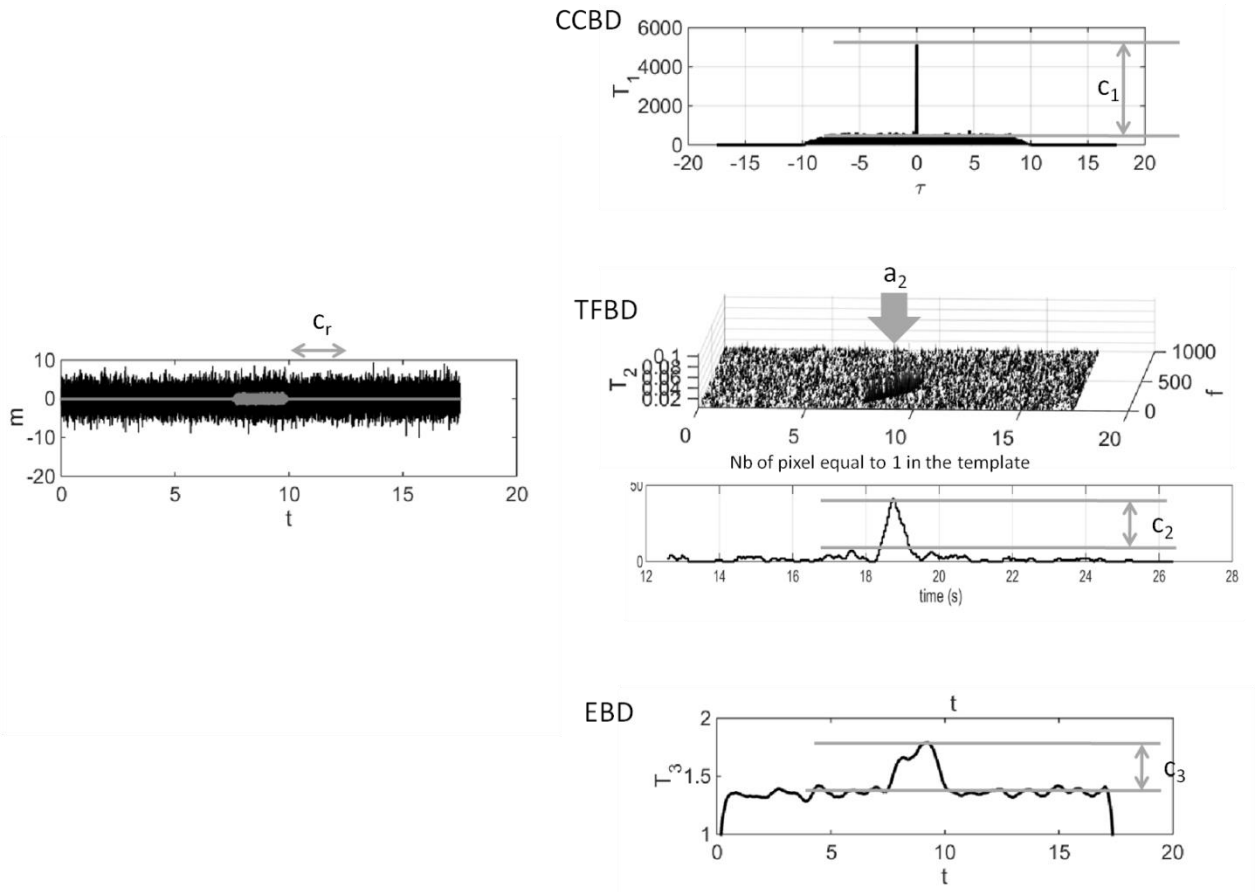

Figure 9. Step qualitative assessment of the detection performance of the three detectors. Left: negative SNR acoustic data, black: noise and upcall; gray: upcall only. Top right: output of CCBD step 2. Middle right: spectrogram of the data and output of TFBD step 2. Bottom right: output of the EBD step 2. The arrows c_1, c_2, c_3 quantify the difference between the noise-only and upcall-present conditions.

Finally, the settings and the degrees of freedom for each detector are presented in Table 4.

Table 4. Settings of the CCBD, TFBD, and EBD detectors.

Setting	Usual values
CCBD	
Step 1 - Reference r(t)	$r(t) = \cos(2\pi f_{min} t + 2\pi \frac{f_{max-fmin}}{2T} t^2)$ T = 1 s, f_{min} = 100 Hz, f_{max} = 200 Hz
Step 2 - Frequency of evaluation of test T1	1 test every 0.1 s
Step 2 - Probability of false alarm	1 per day, 2×10^{-6} per test
TFBD	
Step 1.1: Length of the FFT windows	0.1 s
Step 1: Spectrogram weighting windows	Kaiser 180 dB
Step 1.1: Overlap	50%
Step 1.2: Ambient Noise estimation	Method in Kinda et al. (2013, p. 85-86), percentile = 20.
Step 1.2: Probability of false alarm at the level of the time-frequency bin of the spectrogram	10^{-3}
Step 1.3: Time-frequency template of an upcall	Linear frequency modulation LFM T = 1 s, f_{min} = 100 Hz, f_{max} = 200 Hz Width of the template: ±2 spectrogram time steps around the upsweep time-frequency bin center
Step 2: Frequency of evaluation of test T2	1 test every 0.1 s
Step 2: Probability of false alarm when the template of the upcall is matched with the tested acoustic data	1 per day, 2×10^{-6} per test
EBD	
Step 1.1: bandwidth of the passband filter	[f_{min}, f_{max}] = [100 Hz, 200 Hz]
Step 1.2: Duration of energy integration	T = 1 s
Step 2: Frequency of evaluation of test T3	1 test every 0.1 s
Step 2: Probability of false alarm	1 per day, 2×10^{-6} per test

2.3.5. Receiver Operational Characteristics (P_d, P_{fa}, SNR) of the three detectors

To complete the qualitative approach of CCBD, TFBD, and EBD performances presented in section 2.3.3, we derive here the Receiver Operational Curves (ROC). The ROCs provide a rapid overview of the detection performance. For each detector, the ROC takes the form of an analytically or numerically derived function which links the detection probability, the probability of false alarm and the SNR:

$$ROC <=> P_d = function(P_{fa}, SNR).$$

If we choose to fix the probability of false alarm, the ROC expresses the relation between the detection probability and the SNR. For a given ambient noise (diffuse Wenz's noise and noise from individual ships), source levels and transmission losses, the ROCs are used to:

- quantify the detection probability as a function of whale range,
- quantify the expected detection range corresponding to a given detection probability.

On the first hand, as a detection of an upcall (right or false) will first elicit a validation by an human operator and second a decision about the regulation of the shipping or fishing activity, we want to avoid numerous false alarms and we target a low false alarm probability: 1 false alarm per day or 2×10^{-6} per test.

On the second hand, the PAM systems are used to protect the "endangered" species. So, we target a large probability of detection equal to 50% per test. Choosing a larger probability and at the same time expecting to have only one false alarm per day would cause a drastic increase of the required minimum SNR and a large drop in the range of detection. This level is conformed with the state of the art of the PAM throughout the world as demonstrated during the bench-test of PAM DCLDE international workshop, in 2013 (https://soi.st-andrews.ac.uk/dclde2013/). As the NARWs regularly emit upcalls, the natural and intrinsic redundancy helps improving the hourly or daily probability of detection.

This functioning point is challenging if we expect it still holds at large ranges. Therefore, we propose here a precise and detailed bench-testing of several detectors and PAM systems (single-hydrophone vs hydrophone arrays).

The ROCs of CCBD and EBD under the data assumptions given in section 2.3.2 are classical and we use their expression as given by Kay (1998):

- CCBD: see (Kay 1998, p. 101),
- EBD: see (Kay 1998, p. 250).

The original derivation of ROC for TFBD is fully outlined in annex 2. Table 5 presents the ROCs of CCBD, TFBD, and EBD. One advantage of ROCs of Table 5 is to give a clear and common expression of the SNR for the three types of detectors. These SNRs take into account two components:

- The SNR for raw data: $\frac{A^2}{2\gamma_0}$
- A processing gain (multiplication by T or T_{fft})

- $A/\sqrt{2}$: rms Sound Pressure Level (SPL) of the upcall measured by the receiver
- γ_0: power spectral density of the total noise b_{tot} (diffuse noise and sum of individual ship noises, see section 2.3.2) at the mid frequency of the upcall (150 Hz)
- T: duration of the upcall
- T_{fft}: duration of the FFT windows used to compute the spectrogram
- cdfN: cumulative distribution function of a normal law with mean equal to 0 and variance equal to 1.
- P: number of time-frequency bins (i.e. pixels) of the spectrogram within the upcall time-frequency template
- $\binom{P}{j} = \frac{factorial(P)}{factorial(P-j)\times factorial(j)}$
- ncX2cdf(x,p,q): cumulative distribution function computed at x of a non-central chi^2 law with p degrees of freedom and a parameter of non-centrality equal to q
- $chi^2inv(x,p)$: reciprocal function computed at x of the cumulative distribution function of the centralized chi^2 law with p degrees of freedom.

Table 5. Formula of the ROCs of CCBD, TFBD, and EBD

Detector	**ROC**
CCBD	$\boldsymbol{P_d} = 1 - cdfN(cdfN^{-1}(1-\boldsymbol{P_{fa}}) - \sqrt{\frac{A^2T}{2\gamma_0}})$
TFBD	$\boldsymbol{P_{fa}} = 1 - F_Q(i, H_0)$ $\boldsymbol{P_d} = 1 - F_Q(i, H_1)$ $F_Q(i, H_0) = \sum_{j=0}^{i} \binom{P}{j} (P_{fa\ pix})^j (1-P_{fa\ pix})^{P-j}$ $F_Q(i, H_1) = \sum_{j=0}^{i} \binom{P}{j} (P_{d\ pix})^j (1-P_{d\ pix})^{P-j}$ $P_{d\ pix} = 1 - ncX2cdf(-2\log(P_{fa\ pix}), 2, 0.8\frac{A^2T_{fft}}{2\gamma_0})$
EBD	$P_d = 1 - ncX2cdf(chi2inv(1-P_{fa}, N), N, \frac{A^2T}{2\gamma_0})$

Figure 10 presents the ROCs of the three detectors for an expected P_{fa} equal to 2×10^{-6}. For each detector, the shift from bad detection ($P_d < 0.1$) to very good detection ($P_d > 0.9$) occurs within a 4-dB change in SNR. If spherical spreading loss ($20\log_{10}(r)$) applies, 4 dB corresponds to a change of range by a factor of 1.58. A 58% decrease of the whale range (for example 100 km to 42 km) changes an inefficient detector to an efficient one. To perform as well as TFBD, EBD needs a 12-dB higher SNR, which means that the EBD detection range is 4-times shorter than TFBD range.

Similarly, TFBD requires a 3-dB higher SNR to perform as well as CCBD, which corresponds to a 1.4-time lower detection range (for example 100 km for CCBD compared to 60 km for TFBD).

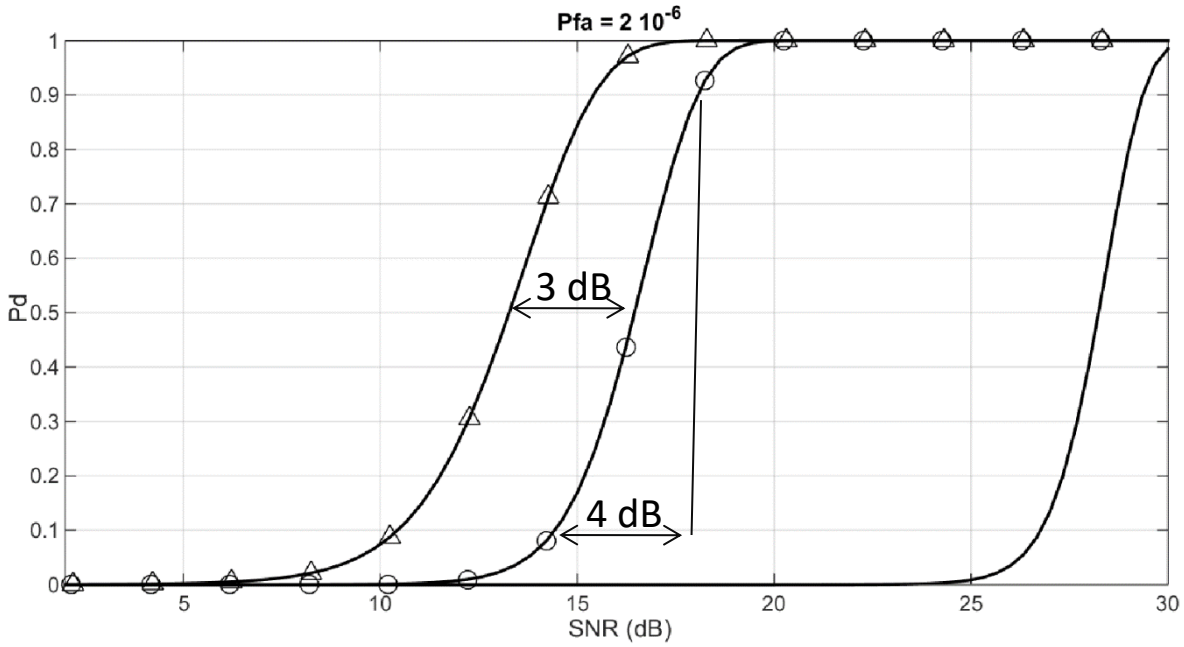

Figure 10. ROCs at $P_{fa} = 2\times10^{-6}$ for the three detectors.
Triangles: CCBD; circles: TFBD; continuous line without symbols: EBD.

2.3.6. Accounting for the use of a hydrophone array

Here, we incorporate the use of a hydrophone array into the computation of ROCs. We assume a planar 2D hydrophone array and a horizontal 2D configuration between the hydrophone array and the different sources of noise, since the range between the sources and the array is much larger than the depth of the acoustic propagation channel. Figure 11 sets the geometry and the conventions. A 2D set of coordinates is used, the x-axis is oriented towards the east and the y-axis towards the north. The azimuth is the angle between the east and the line of sight of the source. A 2D network of N_c hydrophones is placed at location (x_i, y_i) for hydrophone number i. The angle α_w is the azimuth of the whale and α_s is the azimuth of a ship.

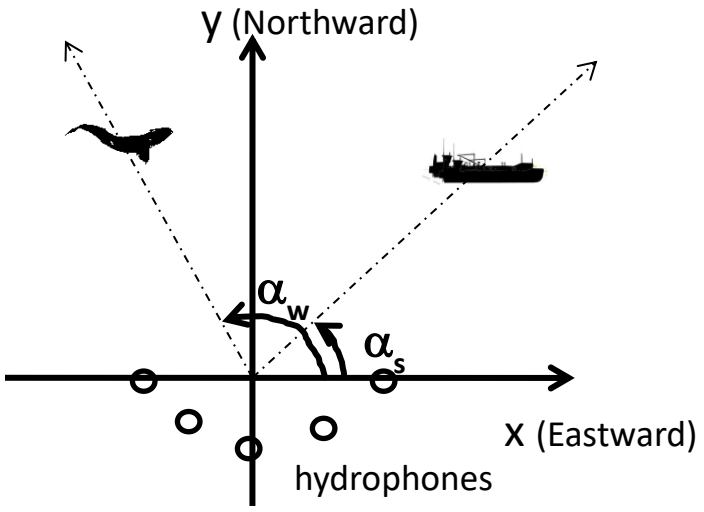

Figure 11. Geometry and conventions used for a hydrophone array.

The measurements of each hydrophone can be linearly combined, the weights applied to each measurement prior to summation allow for tuning the directivity of the hearing towards a preferred direction while drastically decreasing the hearing in the other directions. This succession of weighting and summation is named beamforming (Haykin 1985, For individual items see A85-43961 to A85-43963.). Let be α_2 the preferred azimuth and α_1 the azimuth of a generic source at frequency f, the processing gain of using beamforming is:

$$G(\alpha_2, \alpha_1, f) = \sum_{i=1:N_c} \frac{1}{\sqrt{N_c}} \exp(2\pi j \frac{c}{f}[-(c_i|u_2) + (c_i|u_1)]),$$
$$\text{with } c_i = \begin{pmatrix} x_i \\ yi \end{pmatrix}, u_1 = \begin{pmatrix} -\cos(\alpha_1) \\ -\sin(\alpha_1) \end{pmatrix}, u_2 = \begin{pmatrix} -\cos(\alpha_2) \\ -\sin(\alpha_2) \end{pmatrix}.$$

The processing gain G is such as:

$$|G(\alpha_1, \alpha_1, f|^2 = 1, \ and \ |G(\alpha_2, \alpha_1, f|^2 \leq 1.$$

The wideband beamforming processing gain is computed by:

$$\overline{G^2}(\alpha_2, \alpha_1) = \frac{1}{N_f} \sum_{f \in [f_{min}, f_{max}]} G(\alpha_2, \alpha_1, f).$$

Figure 12 and Figure 13 present the processing gain of the beamforming for a 125-m long, 20-hydrophone linear array and that of a 20-hydrophone circular array with a 20-m radius. For comparison, the radius of the circular array is chosen such that its perimeter is equal to the length of the linear array. The processing gain presents a maximum toward the preferred azimuth, where a main lobe is formed with a width equal to the angular resolution flanked with side lobes. The difference between the gain at the preferred azimuth and other azimuths sets the abilities of the array to focus on the preferred azimuth (the direction of the whale) while filtering out the other azimuths (the direction of the ship). When the preferred azimuth is orthogonal to the linear array, the linear array shows a better angular resolution and weaker side lobes than the circular array. When the preferred azimuth tends to be parallel to the linear array, the resolution of the linear array drops and an ambiguity appears. This does not happen with a circular array, whose response does

not depend on the preferred azimuth. With such hydrophone arrays, the unwanted azimuth signal can drop by at least 15 dB.

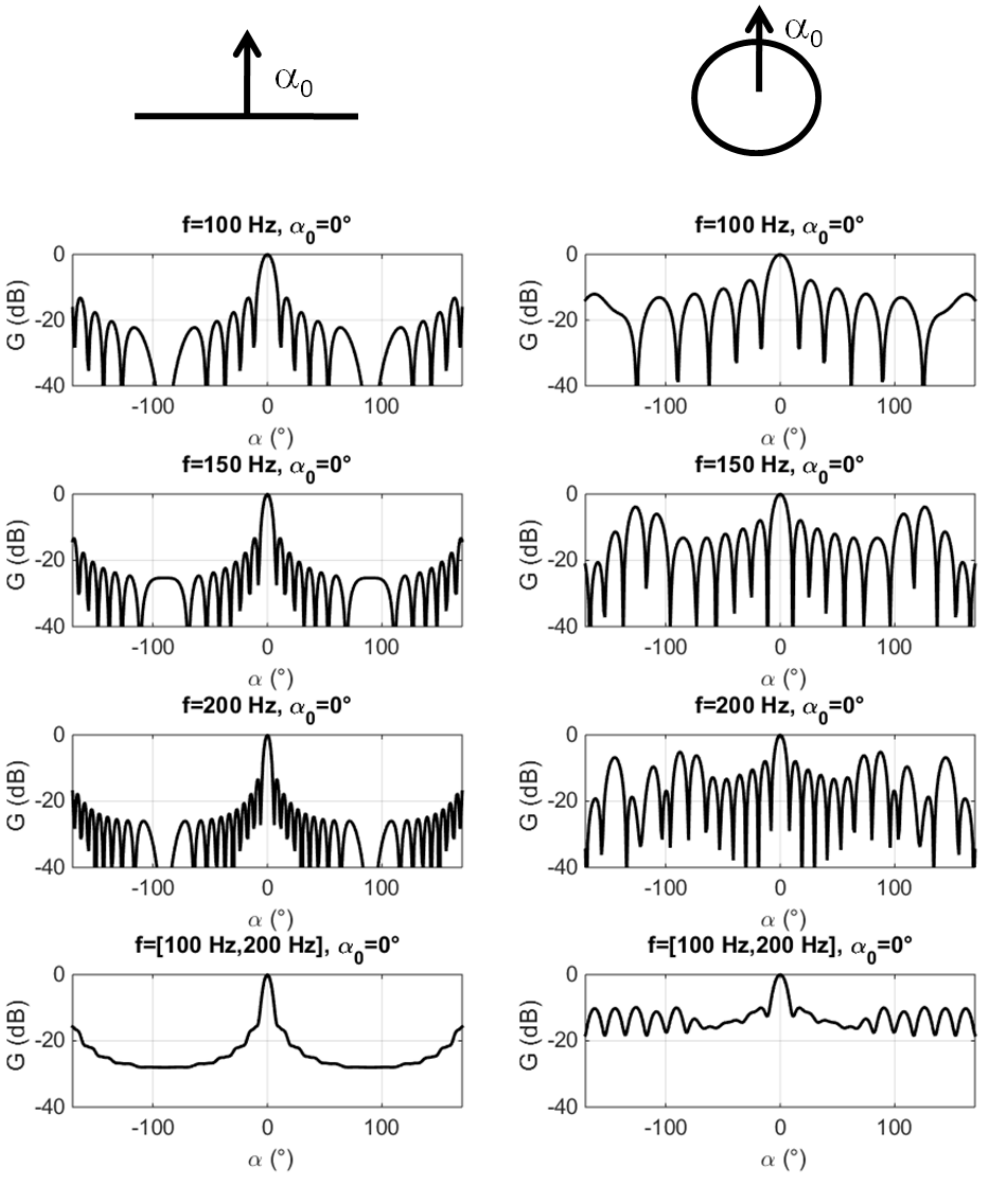

Figure 12. Beamforming processing gain for a preferred direction $\alpha_1 = 0°$.
Left: for a linear array (20 hydrophones, length = 125 m).
Right: for a circular array (20 hydrophones, radius = 20 m).

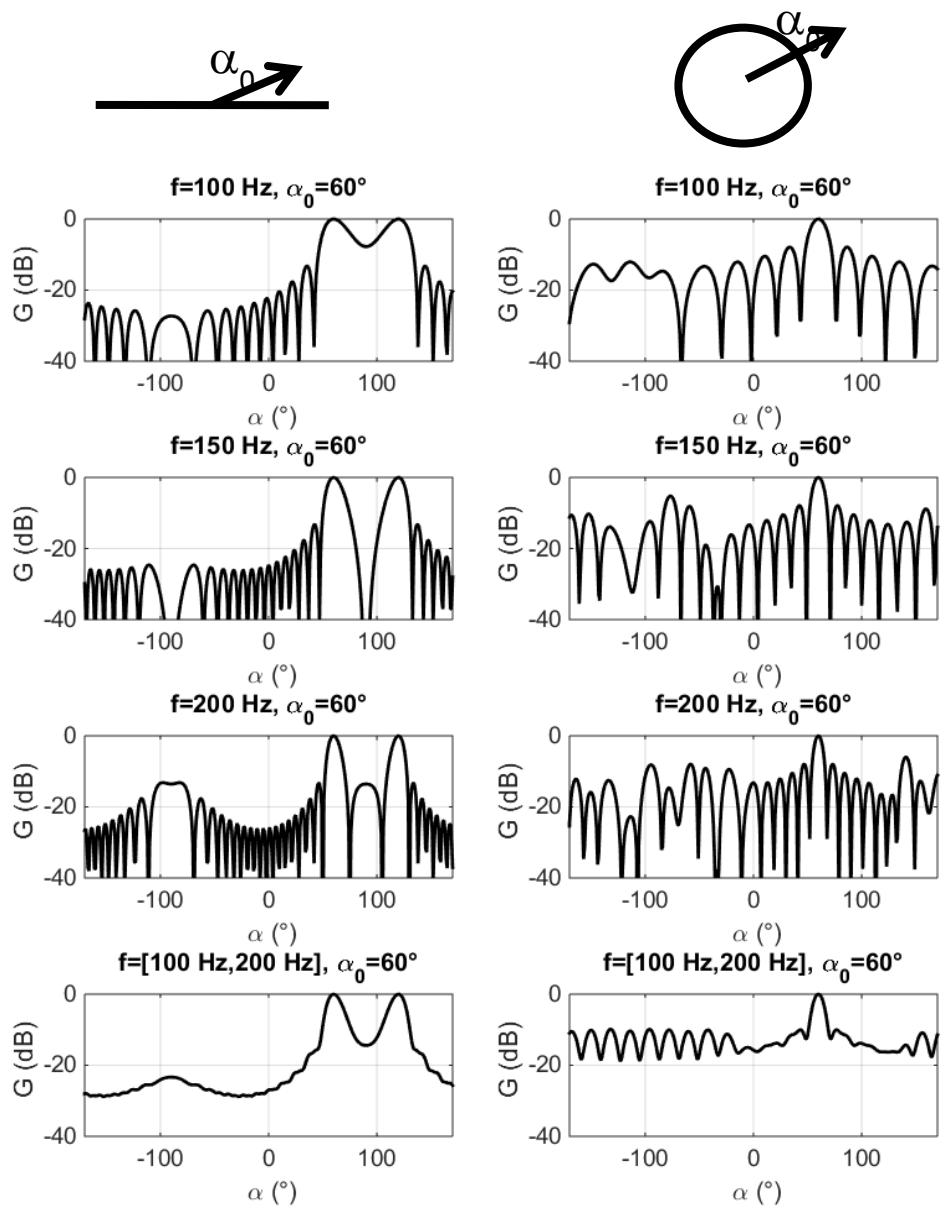

Figure 13. Beamforming processing gain for a preferred direction $\alpha_1 = 60°$.
Left: for a linear array (20 hydrophones, length = 125 m).
Right: for a circular array (20 hydrophones, radius = 20 m).

Let us consider a complex realistic situation with a whale emitting an upcall and several ships radiating their own noises (see Figure 14); the processing gain of the array can be incorporated into the ROC formula by weighting each term of the SNR by its beamforming gain:

$$A_{dB} = SL_w - TL_W - \overline{G_{dB}}(\alpha_w, \alpha_w)$$

$$\gamma_{0_{dB}} = 10log_{10}\left(\sum_{i=1:N} 10^{\frac{\gamma_{SSL}{}^{(i)} - TL_i - \mathrm{G_{dB}}(\alpha_{si}, \alpha_w)}{10}} + 10^{\frac{1}{Nc}\frac{\gamma_{wenz}}{10}}\right),$$

with $\mathrm{G_{dB}}(\theta_1, \theta_2) = 10\log_{10}\left(\overline{G_{dB}(\theta_1, \theta_2)^2}\right)$

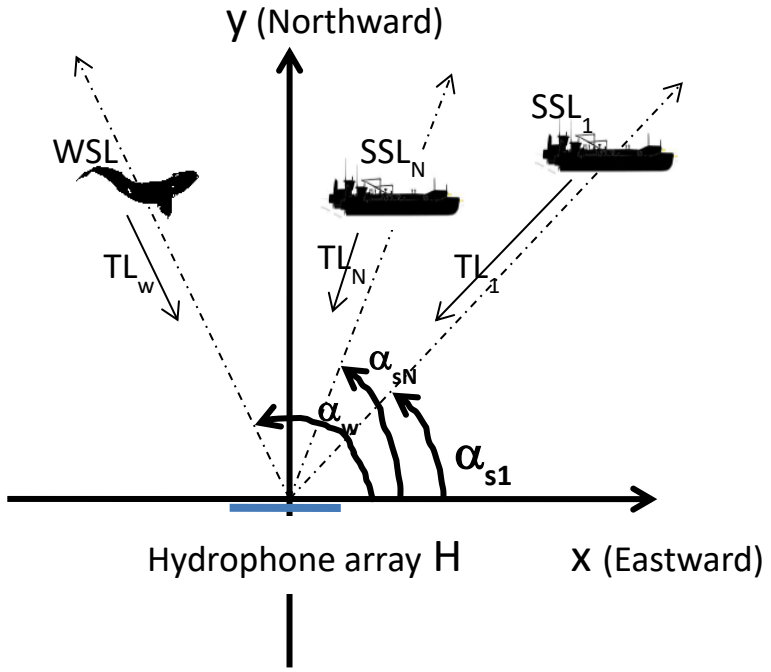

Figure 14. Scenario for a realistic case where a whale at azimuth α_w emits an upcall of source level WSL, the transmission loss to reach the array is TL_w, and several ships at azimuth α_{si} with source levels SSL_i and transmission losses TL_i.

3. RESULTS

3.1. Mapping of the area of 'good detection' within Honguedo strait for 1 year of traffic

3.1.1. Scenario

Here, we explain how we mapped the NARW upcall detection performances of a given PAM system based upon a realistic simulation of year 2017 by steps of 10 minutes, which provides 52 560 acoustical situations.

The TL maps (see section 2.2.4) from the upcall and from a ship to the PAM system were computed for frequencies 100 Hz, 150 Hz, and 200 Hz on a 1 km × 1 km grid over a 100-km radius and stored in memory. The wideband beamforming processing gain for the hydrophone array, $\overline{G^2}(\alpha_2, \alpha_1)$, was computed from -180° to 180° with steps of 1° for the two azimuths α_2 and α_1 and 101 frequencies between 100 Hz and 200 Hz. Results were stored in memory. For a single hydrophone, $\overline{G^2}(\alpha_2, \alpha_1)$ was set to 1.

A random but realistic shipping traffic within the Honguedo dynamic management corridor was simulated for the following conditions:

- 6169 ships for 2017 were considered,
- the times of entrance of each ship in the corridor were randomly distributed over 2017 (uniform distribution),
- each ship is randomly allocated to 1 of the two-way traffic lanes (w_1, w_2, w_3, w_4, see Figure 15) respecting the true proportion of ships in each traffic lane,
- the ship trajectory along the traffic lane follows the true direction with a random 1-km standard deviation around the average traffic lane w_i,
- the transit speed and the narrow band SL (γ_0) of each ship at 150 Hz were randomly chosen following the distribution measured by Simard et al. (2016).

For each sample of the 2017 time series, an instantaneous detection performance is taken by:

- looking for the number, the position, and the SL of ships present in the corridor at this time,
- computing the SNR at this time for each point of the TL grid, thanks to formulas at the end of section 2.3.6,
- computing the detection probability for CCBD, TFBD and EBD and for each point of the TL grid, thanks to the ROC formula (Table 5), fed with $P_{fa} = 2\times10^{-6}$ and the SNR computed at the previous step,
- storing the map of the detection probability of CCBD, TFBD and EBD.

Then the annual time series of the detection maps is summarized in 2 maps:

- map of "wrong functioning", which expresses, for each point of the grid, the proportion of time where pd is less than 0.1,
- map of "right functioning", which expresses, for each point of the grid, the proportion of time where pd is more than 0.5.

Then we propose 2 scalar indicators to rank the map of "right functioning":

- ESD: the Effective Surface of Detection
  - $ESD = \sum_{pixel} Proportion(Pd > 0.5, pixel) dS(pixel)$
- ERD: the Effective Range of Detection
  - $ERD = \sqrt{\frac{ESD}{\pi}}$.

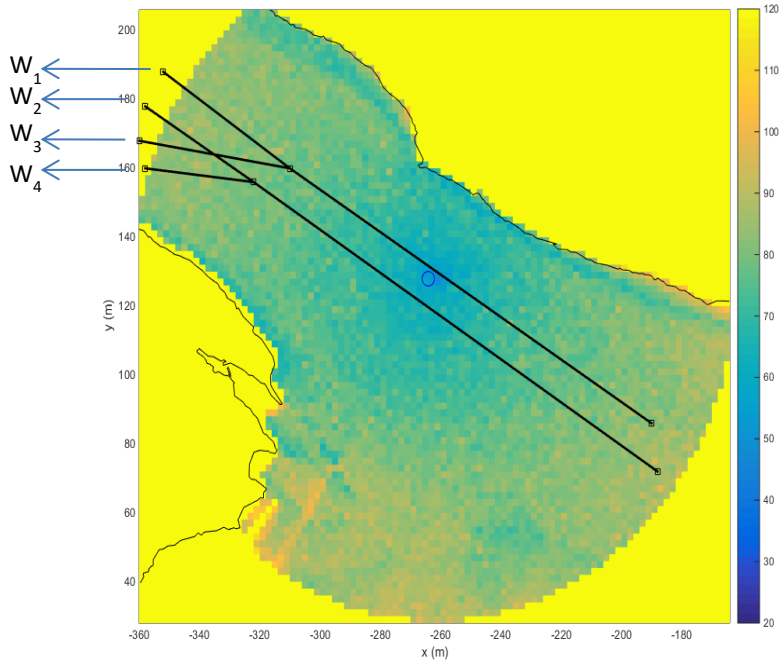

Figure 15. Map of TL (dB) @ 100 Hz between the whale at position (x,y) and a PAM system receiving in the Honguedo position (blue circle).
Black lines: the center of the two-way traffic lanes.

3.1.2. Examples of instantaneous maps of detection probability

Figure 16 sets the pristine detection performance, i.e. with no ship in the dynamic management corridor and only diffuse Wenz noise. The surface where P_d is high covers a large proportion of the corridor surface. Figure 17 presents the case where ships transit within the corridor. The surface of high probability of detection is drastically reduced compared with the pristine case with no traffic. It covers only a small proportion of the corridor. TFBD detection range of detection at the Honguedo PAM system position is about 20 km whereas it seems larger for a PAM system located at Cloridorme. Figure 18 compares the cases of using a single hydrophone and using a 20-m radius circular array of 20 hydrophones. Here 5 ships are present in the corridor and the range of detection with a single hydrophone is close to null. The use of the circular hydrophone array greatly improves the detection, blind areas still exist (see a_1, a_2, a_3, a_4, Figure 18) but they are limited to a 7° cone in the direction of the ships. Figure 19 confirms the advantage of using a hydrophone array versus a single hydrophone at Cloridorme.

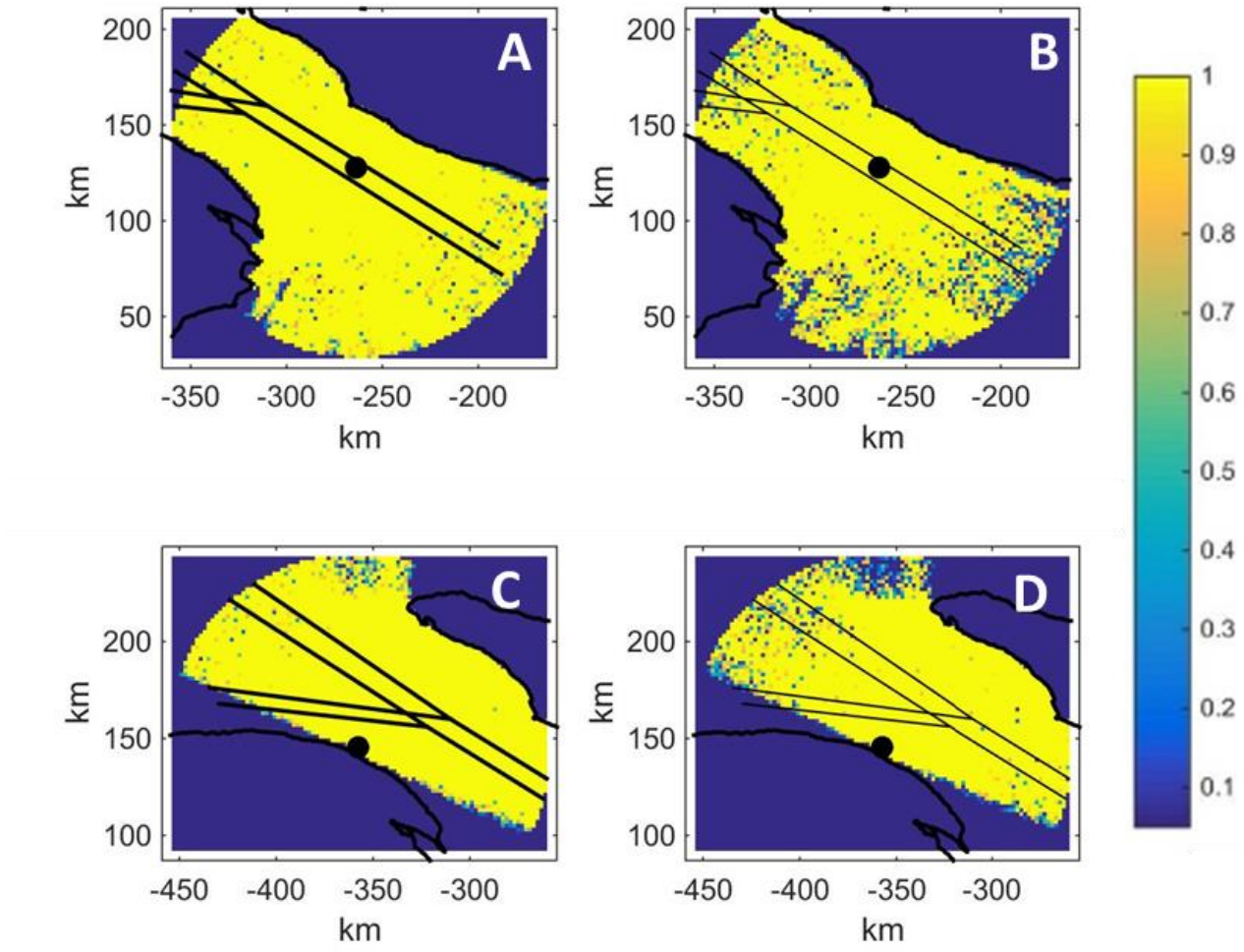

Figure 16. Instantaneous maps of detection probability for 1 single hydrophone receiving at Honguedo (black point, A, B) position, 40 m depth, with a CCBD (A) or a TFBD detector (B), and receiving at Cloridorme (black point, C, D), with a CCBD (C) or a TFBD (D) detector and no ship in the area.

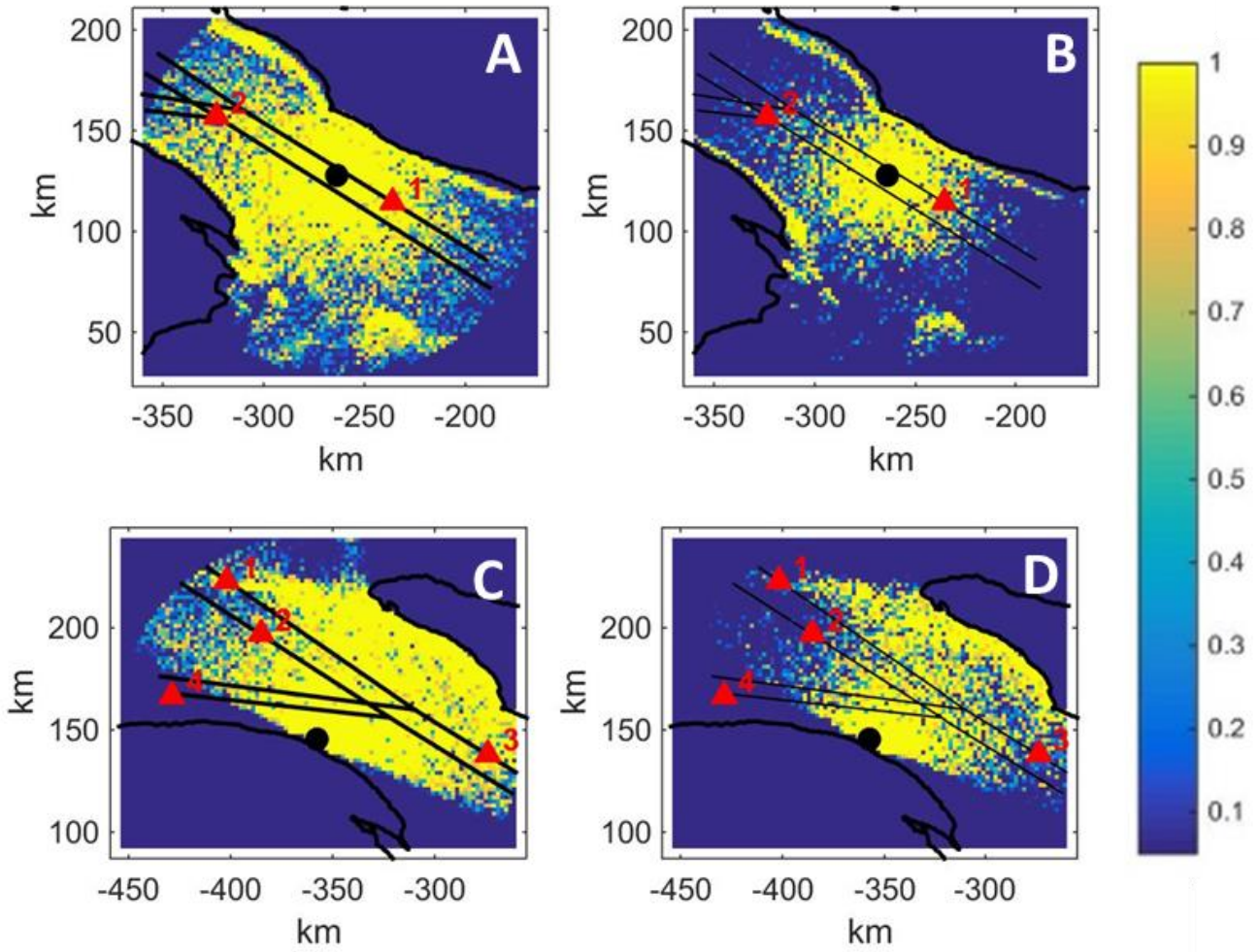

Figure 17. Instantaneous maps of the detection probability for 1 single hydrophone receiving at Honguedo position, 40 m depth, when 2 ships are transiting (red triangles 1, 2), with a CCBD(A) or a TFBD detector (B), and receiving at Cloridorme when 4 ships are transiting (red triangles 1, 2, 3, 4), with a CCBD (C) or a TFBD (B) detectors. For A et B, SL (dB re 1 μPa^2/Hz at 150 Hz) is 146 for ship 1 and 154 for ship 2. For C and D, SL (dB re 1 μPa^2/Hz at 150 Hz) is 153 for ship 1, 157 for ship 2, 155 for ship 3 and 153 for ship 4.

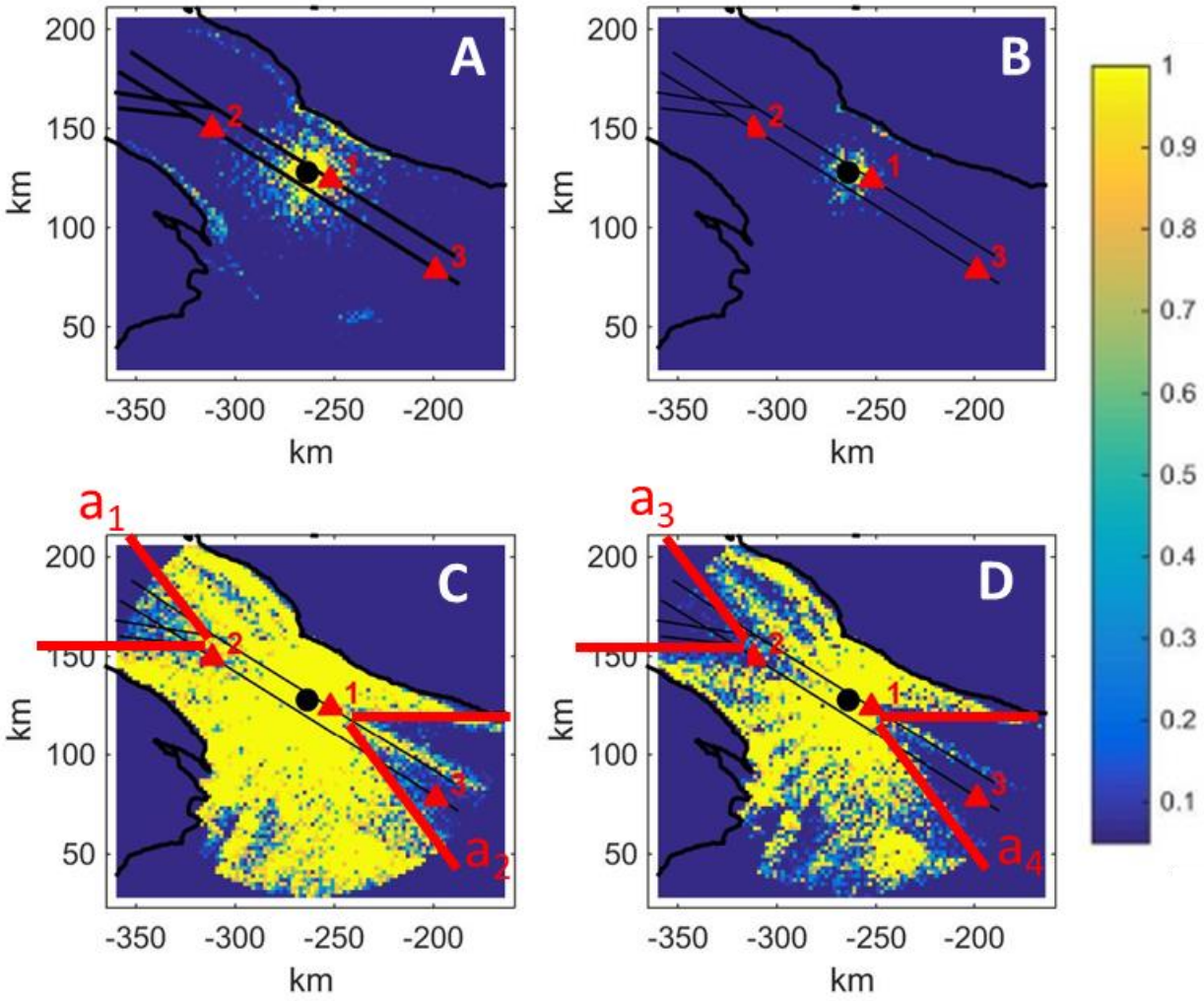

Figure 18. Instantaneous maps of detection probability for 1 single hydrophone receiving at Honguedo position, 40 m depth, when 3 ships are transiting (red triangles 1, 2, 3), with a CCBD (A) or a TFBD detector (B) or receiving with a 20-m radius, 20-hydrophone array, under the same traffic with a CCBD (C) or a TBFD (D) detector.
SL (dB re 1 µPa^2/Hz at 150 Hz) is 146 for ship 1; 154 for ship 2 and 159 for ship 3.

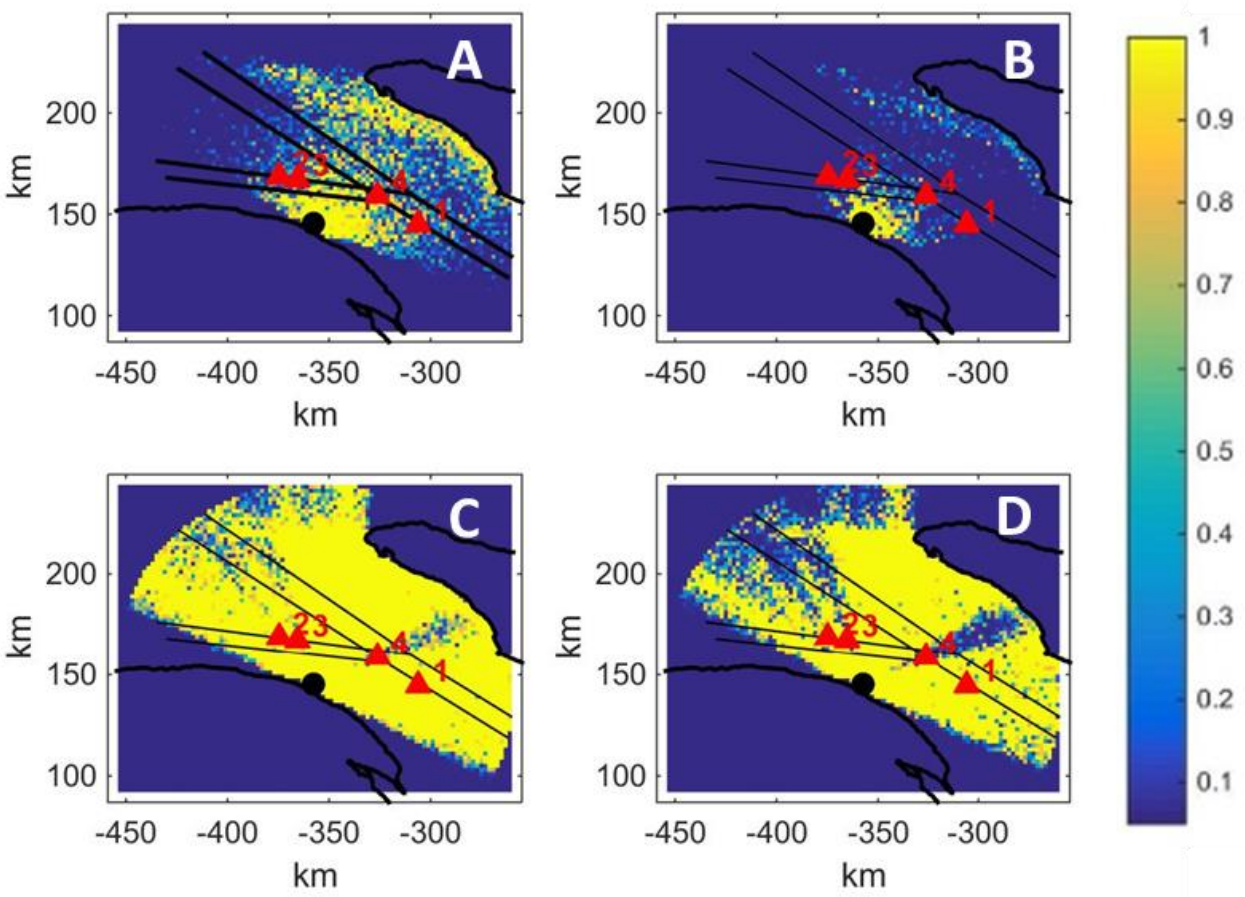

Figure 19. Instantaneous maps of detection probability for 1 single hydrophone receiving at Cloridorme position when 4 ships are transiting (red triangles 1, 2, 3, 4), with a CCBD (A) or a TFBD (B) detector, or receiving with a 20-m radius, 20-hydrophones array, under the same traffic with a CCBD (C) or a TBFD (D) detector.
SL (dB re. 1 $\mu Pa^2/Hz$ at 150 Hz) is 145 for ship 1; 155 for ship2, 155 for ship 3 and 162 for ship 4.

3.1.3. Examples of maps of the area of right and wrong functioning

Figure 20 reports the area of right and wrong functioning for the detection of an upcall at the Honguedo PAM system position for a single hydrophone at 40-m depth. The area of right functioning is small, concentrated around the hydrophone, much narrower than the corridor. This qualitative note is confirmed by calculating the ESD and ERD (see Table 6). Figure 21 draws the comparison between a single hydrophone at Honguedo and Cloridorme; the area of right functioning is improved by placing the sensor at Cloridorme. Figure 22 illustrates the value of using a hydrophone array to increase the size of the area of right functioning that may cover in this case the western half of the corridor with the array at Cloridorme.

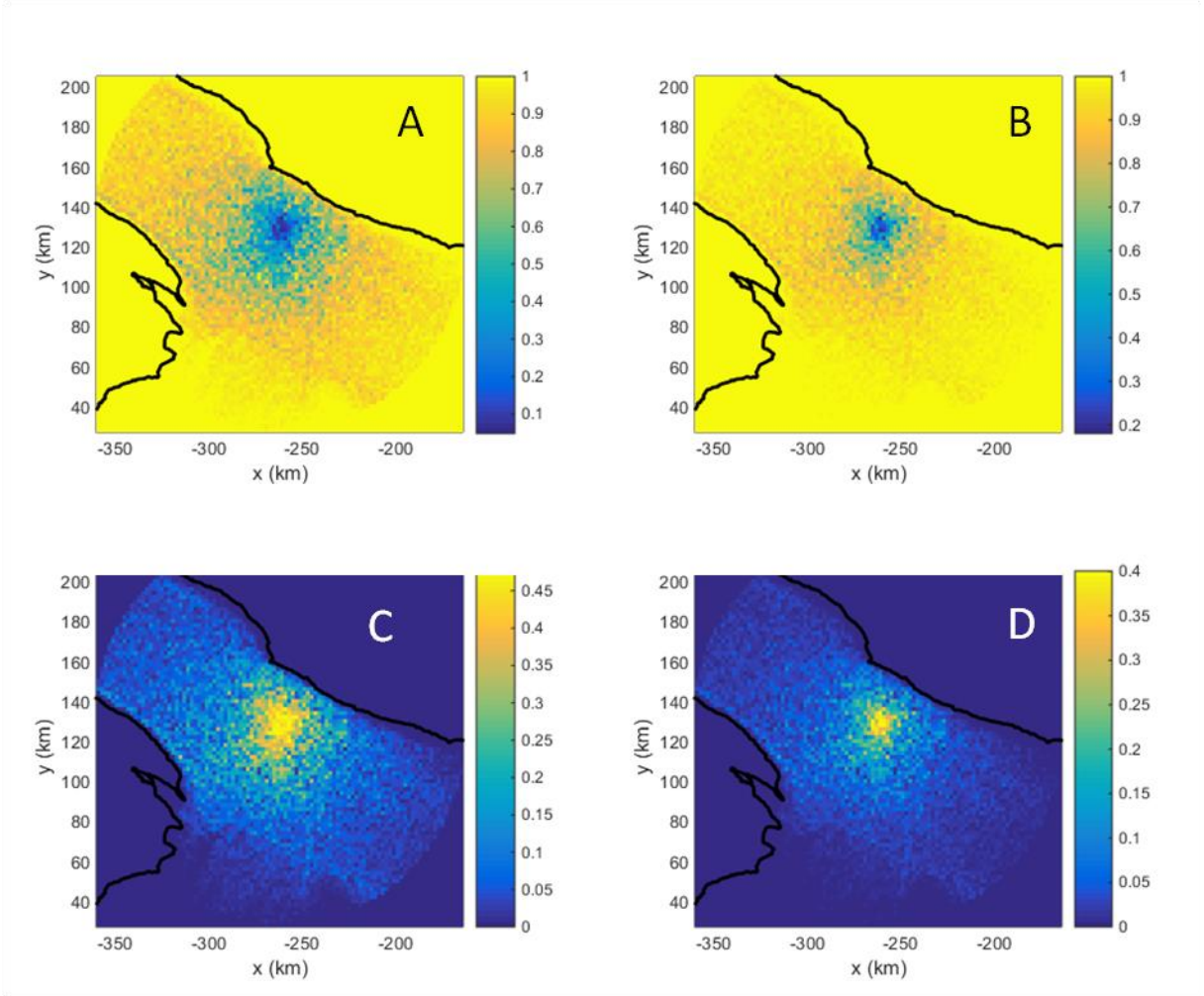

Figure 20. Maps of right and wrong functioning for 1 hydrophone, 40 m depth, at the Honguedo position.
A: CCBD, wrong functioning map (proportion of time pd < 0.1), B: TFBD, wrong functioning map (proportion of time pd < 0.1), C: CCBD, right functioning map (proportion of time pd > 0.5), D: TFBD, right functioning map (proportion of time pd > 0.5).

Table 6. ESD and ERD for detections at Honguedo receiving position, 1 hydrophone, 40 m depth.

	ESD (km^2)	**ERD (km)**
CCBD	1590	22
TFBD	699	14

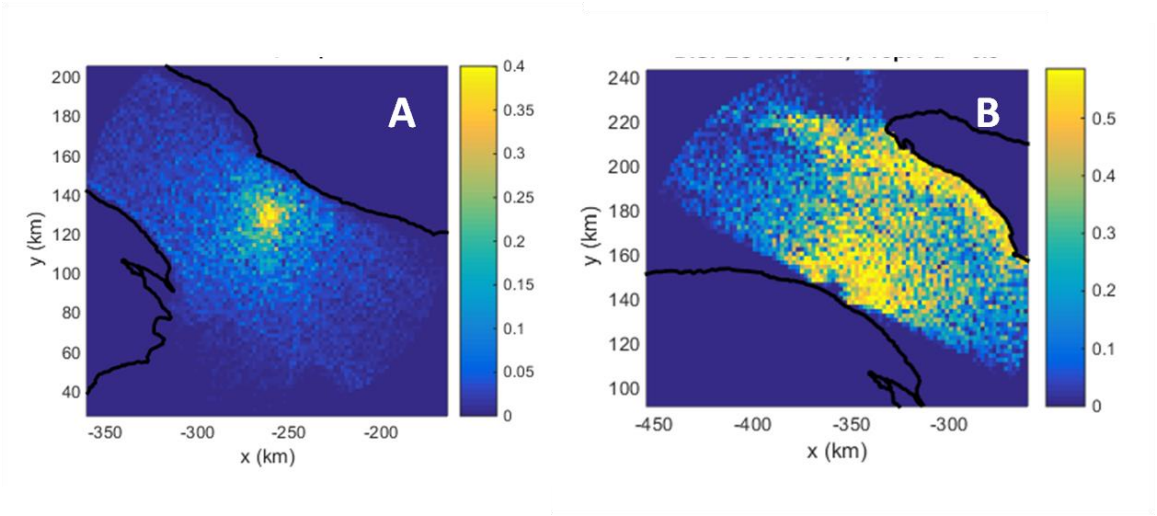

Figure 21. Maps of right functioning (proportion of time $P_d > 0.5$) for 1 hydrophone, A) receiving at Honguedo position, 40-m depth, and B) at Cloridorme.

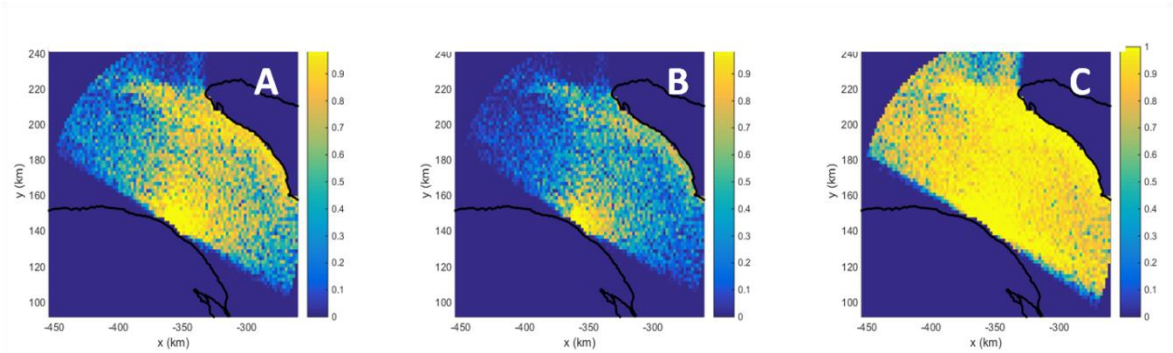

Figure 22. Maps of right functioning (proportion of time $P_d > 0.5$) at Cloridorme, A) with a single hydrophone and CCBD, B) with a single hydrophone and TFBD, and C) with a circular hydrophone array (radius: 20 m, number of hydrophones:20) and TFBD.

3.1.4. Effective Range of Detection for a single hydrophone at Honguedo position

Table 7 reports the ERD for CCBD and TFBD for a single hydrophone at the Honguedo PAM system position. CCBD ERD is 21.5 ±1.14 km and TFBD ERD is 14.25 ± 0.87km. The ERD does not show a high sensitivity to the depth of the hydrophone.

Table 7. ERD for 1 single hydrophone at the Honguedo receiving position and various depths.

Hyd. Depth (m)	20	40	60	80	100	120	140	160	180	200
CCBD	22	22	21	22	22	23	22	22	21	21
TFBD	15	15	14.5	15	15	15	15	15	14	14

Hyd. Depth (m)	220	240	260	280	300	320	340	360
CCBD	21	21	20	20	20	20	19	19
TFBD	14	15	13	13	13	13	15	13

3.1.5. Cloridorme versus Honguedo receiving positions with 1 hydrophone and TFBD

The ERD of a single hydrophone receiving at Cloridorme with TFBD is 32 km, whereas it is 14.25 ±0.87 km at Honguedo (see Figure 21). This highlights the importance of the hydrophone position in the extent of masking by shipping noise. Figure 23 illustrates this using a simple geometrical consideration. As the Honguedo PAM system is located inside the shipping corridor, configurations may exist where a ship is located between the hydrophone and the whale. In such a case, the ship will likely mask the upcall unless it is a very silent ship, because the TL of the ship noise will be considerably smaller than the TL of the whale upcall. For the same ship and whale configuration at the Cloridorme PAM system position, far from the shipping corridor, where detection range is closer to areas of no traffic, the ship and the whale are at equal distances with the hydrophone and the TL for the two sources will be similar; therefore, the risk of a masking the upcall by the ship noise will decrease.

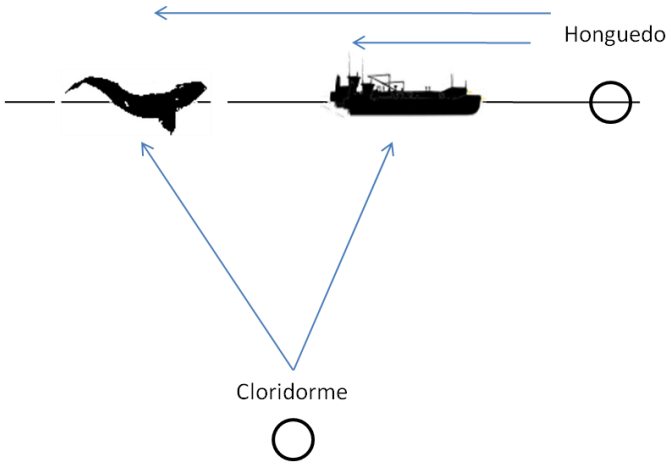

Figure 23. Geometrical consideration to explain masking differences between Honguedo and Cloridome receiving positions.

If we shift the position of the PAM system 25-km south of the corridor, 4 (256/64) hydrophones with TFBD are required to cover the entire ABC dynamic management corridor.

3.1.6. Effective Range of Detection at Cloridorme with a hydrophone array

Table 8 details the ERD of a hydrophone array with TFBD located at Cloridorme. Replacing the single hydrophone by an antenna at Cloridorme multiplies the ERD by a factor 2. The ERD is more than 60 km, even for a small array of 10 hydrophones. The gain of using longer arrays is limited at Cloridorme because the smallest one (10 hydrophones) has an ERD that already reaches the southern coast of Anticosti (see Figure 24)

Table 8. ERD for a hydrophone array receiving at Cloridorme.

Geometry of the array	ERD (km) for TFBD
Honguedo, single hydrophone	14.25 ±0.87
Cloridorme, single hydrophone	32
Cloridorme, linear array (L = 37 m, 10 hyd.)	61
Cloridorme, linear array (L = 125 m, 20 hyd.)	64
Cloridorme, linear array (L = 187 m, 50 hyd.)	66
Cloridorme, circular array (R = 18 m, 10 hyd.)	59
Cloridorme, circular array (R = 20 m, 10 hyd.)	62
Cloridorme, circular array (R = 93 m, 50 hyd.)	66

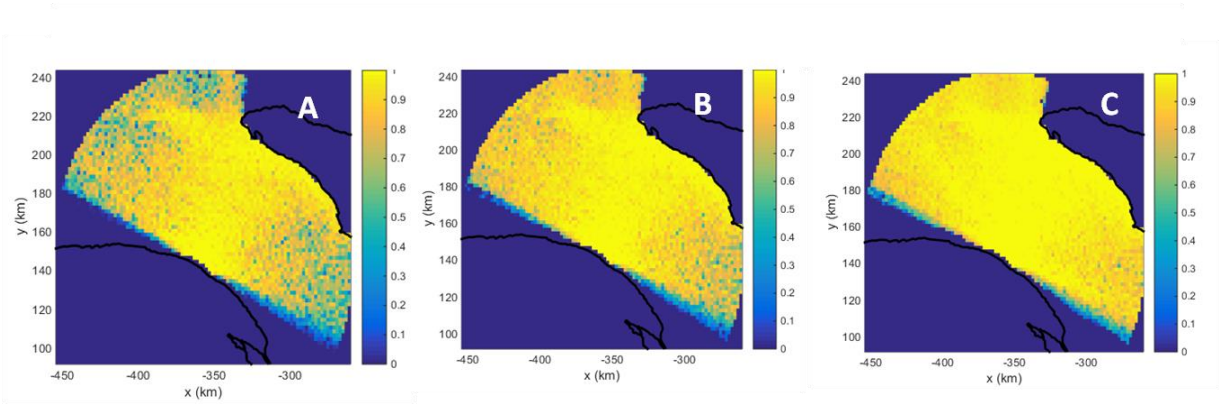

Figure 24. Maps of right functioning (proportion of time pd > 0.5) for a linear hydrophone array of various lengths and TFBD detector.
A: 10 hydrophones, L = 37 m; B: 20 hydrophones, L = 75 m; C: 50 hydrophones, L = 187 m.

4. DISCUSSION

In the present study, we addressed the issue of detecting a NARW upcall within the Honguedo shipping corridor. With its size and mid-traffic conditions (256 km × 60 km, 16 ships per day, 7 ships at the same time in the corridor), the corridor is noisy. The noise is created by discrete localized sources (i.e. the ships transiting in the corridor) and a hydrophone array may be used to filter out these punctual sources by beamforming to enhance the upcall SNR, its detection probability and range.

4.1. Choosing the right detector and needs for a precise map of detection performance

We considered 3 detector types for the upcall and we carefully derived the ROCs. The CCBD sets the best detection performance bounds but lacked robustness and it requires large computational capacities. EBD is basic and sets the worst detection performance bounds. TFBD

represents the state of the art used in present operational PAM systems. A common expression for SNR is shared by the three ROCs, permitting a precise comparison between the three detectors.

If the probability of false alarm is set to one per 24 h (i.e. probability of false alarm equal to 2×10^{-6} per test, one test every 0.1 second), a SNR variation of 4.23 ± 1.06 dB can shift from bad detection performance (P_d equal to 0.1) to very good performance (P_d equal to 0.9). Such SNR variation can be observed when the distance between the hydrophone and the calling whale increases. For instance, assuming spherical TL in first approximation, if bad detection performances are observed at a range d = 100 km, the detection performance becomes very good at 61 km (= 0.61d). The range shift from bad to very good detection performances occurs over a distance of only 39 km, which is the scale of the ABC dynamic management corridor. Therefore, the detection performance could be good in one part of the corridor and bad in the adjacent part. Precise mapping of the detection probability is thus necessary to properly assess acoustic system detection performance.

A detection probability of 50% and one false alarm per 24 h are chosen as realistic functioning point of the acoustic detection system. To obtain this functioning point, minimum SNRs are 13.27 dB for CCBD, 16.43 dB for TFBD and 28.15 dB for EBD. Therefore, using spherical TL in first approximation, the maximum detection ranges, r_{CCBD}, r_{TFBD}, $r_{EBD,}$ correspond to the minimum necessary SNR for CCBD, TFBD, and EBD, and we can express r_{TFBD} and r_{EBD} with respect to r_{CCBD} as:

- $r_{EBD} = 10^{-(28.15-13.27)/20} r_{CCBD} = 0.18 r_{CCBD}$
- $r_{TFBD} = 10^{-(16.43-13.27)/20} r_{CCBD} = 0.72 r_{CCBD}$.

Using the basic EBD would decrease by 82 % the detection range obtained with the optimal CCBD. Considering this poor detection performance, EBD is definitely rejected.

The level of performance is proportional to the level of the *a priori* knowledge used by the detectors. EBD requires only knowing the bandwidth of the upcall, TFBD requires knowing a time-frequency template of the upcall, whereas CCBD needs the precise full waveform template.

Using the operational, robust and real-time-compatible TFBD decreases the detection range by only 28 % compared to the optimal, but not robust and not real-time compatible, CCBD range. Indeed, the optimality of CCBD is guaranteed by a perfect knowledge of the upcall at the receiver. However, in practice, it is impossible to possess this level of *a priori* knowledge, because the source itself is subject to some variability in its structuring features (e.g. minimum frequency, maximum frequency, duration, …). This intrinsic variability is magnified by the propagation within shallow waters, which introduces several distortions of the emitted signal. The propagated signal may include several echoes. Each echo corresponds to one propagation mode and its time-frequency support is modified by modal dispersion (Gervaise et al. 2008, Ioana et al. 2010). In annex 3, we studied the loss in processing gain of using the CCBD with a wrong reference. We showed that a small 10% deviation of signal duration, minimum or maximum frequencies degraded the SNR by 3 dB, (which is very close to the SNR variation necessary to shift from very good to bad detection performance). In addition, CCBD is more computational demanding that TFBD, which may create difficulties for integrated real-time applications. For these reasons, we conclude that TFBD is a very good trade-off between optimality and operability. We have shown that the range of good

functioning of TFBD is within the scale of the ABC Honguedo dynamic management corridor, which confirms the usefulness of mapping the detection probability.

4.2. Mapping detection performance through the realistic simulation of year 2017

We divided year 2017 in 52 560 steps of 10 min. For each step, we mapped the detection probability of CCBD, EBD with or without beamforming, using an acoustics simulation fed with the realistic TL, ship and upcall SLs, and the true AIS traffic. Then we summed up the one year time series by mapping the area of right functioning (locations within the corridor where the proportion of time pd > 0.5 if more than 50%). Effective Range of Detection and Effective Surface of Detection are evaluated from the area of right functioning.

4.3. Effective Range of Detection for a single hydrophone and TFBD

The ERD of a single hydrophone-TFBD PAM system, located at the Honguedo position, is 14.25 km ± 0.87. The ERD is relatively constant over the receiving depth of the PAM system. Even if the depth of the hydrophone may affect the TL, it similarly affects both the transmission of the whale upcall and the ship radiated noise, so SNR does not change. This configuration covers both the case of one hydrophone mounted on a fixed buoy and a glider. As the length of the corridor is 256 km, 10 hydrophones (~256/28) with TFBD are required to cover the entire corridor (see Figure 25). Because it requires 10 stations, the implementation of this solution for a real-time and complete coverage of the corridor would be expensive and hard to exploit, while also representing a threat to navigation. However, PAM Buoys are operating in real-time for NARW upcall detections in GSL (SLGO, Viking-WOW OOS, https://ogsl.ca/en), taking advantage of an existing set of DFO oceanographic buoys.

One of the causes of this small ERD at Honguedo position is its proximity to the seaway, since there are many instances where individual ships are closer to the hydrophone than the whale (see Figure 23). Then the upcall is masked by the ship noise and the probability of detection is null. As the shipping is concentrated on seaways, moving the hydrophone away from these seaways reduces the difference between the ship and whale ranges. A single hydrophone-TFBD PAM system located at Cloridorme experiences an ERD of 32 km compared to 14.25 ± 0.87 km at the Honguedo position. Therefore, choosing the right location of a single hydrophone TFBD PAM system potentially increases the ERD by a factor of 2 and the ESD by a factor of 4.

4.4. Effective Range of Detection with a hydrophone array and TFBD

As the noise that affects NARW upcall detection is created by punctual ships at their respective positions, NARW upcalls and ship noise do not come from the same direction. A hydrophone array with beamforming allows for directional listening. More precisely, a circular array (20-m radius, 20 hydrophones) is able to focalize in one direction with a resolution of 7° and filter out the other directions by 15 dB within the bandwidth of the NARW upcall (see Figure 12, Figure 13). This additional 15-dB SNR offered by the beamforming increases the detection range by a factor of 5 for spherical TL approximation. We tested multiple configurations of the

hydrophone arrays at Cloridorme. The ERD is around 60 km even for an array of only 10 hydrophones, which exceeds the distance between Anticosti Island and Cloridorme. In that configuration, the ERD is floored by the Honguedo strait width and half of the ABC corridor length is covered.

4.5. Extension of the results

Our results may be extended without extra computation:

- the whole surface of the ABC dynamic management corridor can be covered by 2 hydrophone arrays: the first one located at Cloridorme and the second one on the south-east coast of Anticosti Island;
- the D dynamic management corridor may be covered by one hydrophone array located on the GSL north coast or the north coast of Anticosti Island.

4.6. Other gains offered by a hydrophone array

A hydrophone array can estimate the azimuth of the NARW upcall, which may be used to estimate the number of NARWs in the area covered by the PAM system (1 azimuth per whale). If one array is located at Cloridorme and another one on Anticosti, this provides two azimuths for each upcall detection, which then may be crossed to locate the upcall within about half of the ABC dynamic management corridor surface.

While beamforming is used to listen to the upcalls, post-processing can redirect the orientation of the beams towards the ships, providing data that can be used to collect the ship SLs, even with a PAM device that is distant from the traffic.

4.7. Operational conclusions: toward an *ad hoc* PAM system to detect NARW

Ten PAM systems with one single hydrophone are required to cover the ABC Honguedo dynamic management corridor if they are installed within the corridor itself, whereas five of them are required if they are located at the southern border of Honguedo strait. Such configurations would suffer from important masking of upcalls by shipping noise. Also, each surface buoy would represent a threat to navigation; equipment costs, as well as seasonal deployment for the ice-free season and maintenance costs should be high. In addition, real-time access to the data may be expensive for these offshore locations where satellite communication is the only option.

An optimized hydrophone array (20 hydrophones on a 20-m radius circular array, or on a 37-m long linear array) located at Cloridorme covers half of the Honguedo strait and provides the azimuth of the upcalls. This near-shore station decreases the cost for deployment and maintenance, besides allowing year-round operation. The array is cabled to a terrestrial station providing the power, data processing and real-time broadcast of the detections.

Whereas a hydrophone array may be seen as a complex system, the solution may be cost effective when compared with 10 or 5 buoys discussed above (see Table 9).

We believe using a PAM system with a hydrophone array at Cloridorme should be considered first to optimize the detection of NARW in the Honguedo strait of GSL.

Table 9. Cost efficiency of a PAM system with a hydrophone array vs single hydrophone buoys.

Item	**One array at Cloridorme (20 hydrophones, radius 20 m)**	**10 buoys in Honguedo strait**
Hydrophones	Purchase of 20 units	Purchase of 10 units
Structure	1 support for the hydrophones and ~1 500 m long cable	10 telecommunicating instrumented buoys and 10 moorings
Deployment	Near shore	Offshore
Maintenance	Near shore	Off shore
Batteries for the supply of power	No need	High need
Data processor	Purchase of 1	Purchase of 10
Computational resources	High	Moderate
Real-time	Easy, cheap	Difficult, costly
Season of operability	Year-round	Ice-free

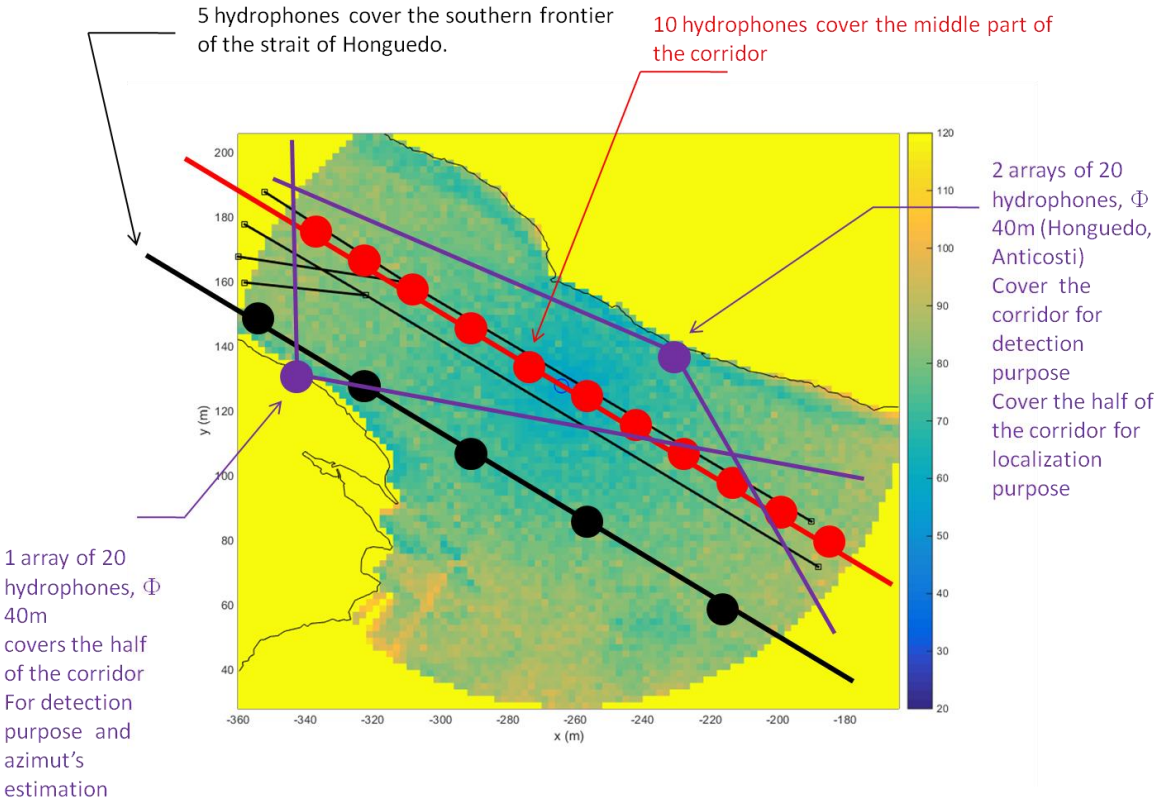

Figure 25. Synthesis of PAM system requirements to detect NARW upcalls in the dynamic management sectors A, B, and C in Honguedo strait.

ACKNOWLEDGMENTS

This work was supported by Fisheries and Oceans Canada. Thanks to Innovation Maritime for AIS traffic density statistics in dynamic management sectors. We are grateful to Bazile Kinda and Jérôme Mars for reviewing the manuscript and to Denis Chabot for his editorial work.

REFERENCES

Abramowitz, M., and Stegun, I. 1974. Handbook of mathematical functions with formulas, graphs and mathematical tables. Dover Publications, Inc., New York, NY, USA.

Aulanier, F., Simard, Y., Roy, N., Bandet, M., and Gervaise, C. 2016a. Groundtruthed probabilistic shipping noise modeling and mapping: Application to blue whale habitat in the Gulf of St. Lawrence, Acoust. Soc. Am. Proc. Meetings Acoust., 27, 070006, pp. 1-14.

Aulanier, F., Simard, Y., Roy, N., Gervaise, C., and Bandet, M. 2016b. Spatio-temporal exposure of blue whale habitats to shipping noise in St. Lawrence system. DFO Can. Sc. Advis. Sec. Res. Doc. 2016/090, p. vi + 26 p.

Aulanier, F., Simard, Y., Roy, N., Gervaise, C., and Bandet, M. 2017. Effects of shipping on marine acoustic habitats in Canadian Arctic estimated via probabilistic modeling and mapping. Mar. Poll. Bull. **125**(1): 115-131.

Baumgartner, M.F., Fratantoni, D.M., Hurst, T.P., Brown, M.W., Cole, T.V.N., Van Parijs, S.M., and Johnson, M. 2013. Real-time reporting of baleen whale passive acoustic detections from ocean gliders. J. Acoust. Soc. Am. **134**(3): 1814-1823.

Baumgartner, M.F., and Mussoline, S.E. 2011. A generalized baleen whale call detection and classification system. J. Acoust. Soc. Am. **129**(5): 2889-2902.

Clark, C., Ellison, W., Hatch, L., Merrick, R., Van Parijs, S., and Wiley, D. 2011. An ocean observing system for large-scale monitoring and mapping of noise throughout the Stellwagen Bank National Marine Sanctuary. Reports to the National Oceanographic Partnership Program, Stellwagen project, Award number N00014-07-1-1029, p. 11 pp.

Clark, C.W. 1982. The acoustic repertoire of the Southern right whale, a quantitative analysis. Animal Behaviour **30**(4): 1060-1071.

Clark, C.W., Brown, M.W., and Corkeron, P. 2010. Visual and acoustic surveys for North Atlantic right whales, *Eubalaena glacialis*, in Cape Cod Bay, Massachusetts, 2001-2005: Management implications. Mar. Mam. Sci. **26**(4): 837-854.

Cole, T.V.N., Hamilton, P., Henry, A.G., Duley, P., Pace III, R.M., White, B.M., and Frasier, T. 2013. Evidence of a North Atlantic right whale *Eubalaena glacialis* mating ground. End. Sp. Res. **21**: 55-64.

Collins, M.D. 1993. A split-step Padé solution for the parabolic equation method. J. Acoust. Soc. Am. **94**(4): 1736-1742.

Dadouchi, F., Gervaise, C., Ioana, C., Huillery, J., and Mars, J.I. 2013. Automated segmentation of linear time-frequency representations of marine-mammal sounds. J. Acoust. Soc. Am. **134(3)**(3): 2546–2555.

Daoust, P.-Y., Couture, E.L., Wimmer, T., and Bourque, L. 2017. Incident Report: North Atlantic right whale mortality event in the Gulf of St. Lawrence, 2017. Collaborative Report produced by: Canadian Wildlife Health Cooperative, Marine Animal Response Society, and Fisheries and Oceans Canada, p. 224 pp.

Davis, G.E., Baumgartner, M.F., Bonnell, J.M., Bell, J., Berchok, C., Bort Thornton, J., Brault, S., Buchanan, G., Charif, R.A., Cholewiak, D., Clark, C.W., Corkeron, P., Delarue, J., Dudzinski, K., Hatch, L., Hildebrand, J., Hodge, L., Klinck, H., Kraus, S., Martin, B., Mellinger, D.K., Moors-Murphy, H., Nieukirk, S., Nowacek, D.P., Parks, S., Read, A.J., Rice, A.N., Risch, D., Širović, A., Soldevilla, M., Stafford, K., Stanistreet, J.E., Summers, E., Todd, S., Warde, A., and Van Parijs, S.M. 2017. Long-term passive acoustic recordings track the changing distribution of North Atlantic right whales (*Eubalaena glacialis*) from 2004 to 2014. Sci. Rep. **7**(1): 13460.

DFO. 2014. Recovery strategy for the North Atlantic right whale (*Eubalaena glacialis*) in Atlantic Canadian waters [Final]. Species at Risk Act Recovery Strategy Series, p. vii +68 pp.

DFO. 2018. Science advice on timing of the mandatory slow-down zone for shipping traffic in the Gulf of St. Lawrence to protect the North Atlantic right whale. DFO Can. Sci. Advis. Sec. Sci. Resp. 2017/042, p. 16 p.

DFO. 2019. Fishing closures for North Atlantic right whale protection: 2019 North Atlantic right whale management measures. Available from http://www.dfo-mpo.gc.ca/fisheries-peches/commercial-commerciale/atl-arc/narw-bnan/index-eng.html [accessed 2019-05-23 2019].

Gervaise, C., Vallez, S., Stephan, Y., and Simard, Y. 2008. Robust 2D localization of low-frequency calls in shallow waters using modal propagation modelling. Can. Acoust. **36**(1): 153-159.

Gillespie, D. 2004. Detection and classification of right whale calls using an "edge" detector operating on a smoothed spectrogram. Can. Acoust. **32**(2): 39-47.

Grieve, B.D., Hare, J.A., and Saba, V.S. 2017. Projecting the effects of climate change on Calanus finmarchicus distribution within the U.S. Northeast Continental Shelf. Sci Rep **7**(1): 6264.

Haykin, S. 1985. Array signal processing. Prentice-Hall, Inc., Englewood Cliffs, NJ.

Ioana, C., Jarrot, A., Gervaise, C., Stéphan, Y., and Quinquis, A. 2010. Localization in underwater dispersive channels using the time-frequency-phase continuity of signals. . IEEE Transactions on Signal Processing **58**(8): 4093–4107.

Kay, S.M. 1998. Fundamentals of statistical signal processing, Vol. II: Detection Theory Prentice Hall, Upper Saddle River, NJ.

Kinda, G.B., Simard, Y., Gervaise, C., Mars, J.I., and Fortier, L. 2013. Under-ice ambient noise in Eastern Beaufort Sea, Canadian Arctic, and its relation to environmental forcing. J. Acoust. Soc. Am. **134**: 77-87.

Lampert, T.A., and O'Keefe, S.E.M. 2010. A survey of spectrogram track detection algorithms. Appl. Acoust. **71**(2): 87-100.

Loring, D.H., and Nota, D.J.G. 1973. Morphology and sediments of the Gulf of St. Lawrence. Bull. Fish. Res. Bd. Can. **182**: 147 p. + 147 charts.

Matthews, J.N., Brown, S., Gillespie, D., Johnson, M., McLanaghan, R., Moscrop, A., Nowacek, D., Leaper, R., Lewis, T., and Tyack, P. 2001. Vocalisation rates of the North Atlantic right whale (*Eubalaena glacialis*). J. Cetacean Res. Manag. **3**(3): 271-282.

Mellinger, D.K., Nieukirk, S.L., Matsumoto, H., Heimlich, S.L., Dziak, R.P., Haxel, J., Fowler, M., Meinig, C., and Miller, H.V. 2007. Seasonal occurrence of North Atlantic right whale (*Eubalaena glacialis*) vocalizations at two sites on the Scotian Shelf. Mar. Mamm. Sci. **23**(4): 856-867.

Meyer-Gutbrod, E.L., and Greene, C.H. 2018. Uncertain recovery of the North Atlantic right whale in a changing ocean. Global Change Biol. **24**(1): 455-464.

Meyer-Gutbrod, E.L., Greene, C.H., and Davies, K.T.A. 2018. Marine species range shifts necessitate advanced policy planning: The case of the North Atlantic right whale. Oceanography **31**(2): 19-33.

Munger, L.M., Wiggins, S.M., and Hildebrand, J.A. 2011. North Pacific right whale up-call source levels and propagation distance on the southeastern Bering Sea shelf. The Journal of the Acoustical Society of America **129**(6): 4047-4054.

Mussoline, S.E., Risch, D., Hatch, L.T., Weinrich, M.T., Wiley, D.N., Thompson, M.A., Corkeron, P.J., and Van Parijs, S.M. 2012. Seasonal and diel variation in North Atlantic right whale up-calls: implications for management and conservation in the northwestern Atlantic Ocean. Endang. Species Res. **17**(1): 17-26.

NRC. 2003. Ocean noise and marine mammals. National Academy Press, Washington D.C.

Parks, S.E., Hotchkin, C.F., Cortopassi, K.A., and Clark, C.W. 2012. Characteristics of gunshot sound displays by North Atlantic right whales in the Bay of Fundy. J. Acoust. Soc. Am. **131**(4): 3173-3179.

Parks, S.E., Searby, A., Célérier, A., Johnson, M.P., Nowacek, D.P., and Tyack, P.L. 2011. Sound production behavior of individual North Atlantic right whales: implications for passive acoustic monitoring. Endang. Species Res. **15**: 63-76.

Parks, S.E., and Tyack, P.L. 2005. Sound production by North Atlantic right whales (*Eubalaena glacialis*) in surface active groups. J. Acoust. Soc. Am. **117**(5): 3297-3306.

Pettis, H.M., Pace, R.M.I., and Hamilton, P.K. 2018. North Atlantic Right Whale Consortium 2018 annual report card. Report to the North Atlantic Right Whale Consortium, p. 17 pp.

Senneville, S., and Lefaivre, D. 2015. Reproduction horaire et à trois dimensions des conditions hydrographiques et hydrodynamiques du Golfe du Saint-Laurent avec le modèle MoGSL pour la période de 1997 à 2014. *In* Rapport 2014-2015 de l'entente de contribution entre le MPO et l'ISMER/UQAR pour la simulation numérique des océans. Fisheries and Oceans Canada, Mont-Joli, QC.

Simard, Y., Roy, N., Gervaise, C., and Giard, S. 2016. Analysis and modeling of 255 source levels of merchant ships from an acoustic observatory along St. Lawrence Seaway. J. Acoust. Soc. Am. **140**(3): 2002-2018.

Simard, Y., Roy, N., Giard, S., and Aulanier, F. 2019. North Atlantic right whale shift to the Gulf of St. Lawrence in 2015 as monitored by long-term passive acoustics. End. Sp. Res. **xx**: xxx-xxx.

Simard, Y., Roy, N., Giard, S., and Yayla, M. 2014. Canadian year-round shipping traffic atlas for 2013: Volume 1, East Coast marine waters. Can. Tech. Rep. Fish. Aquat. Sci. 3091(Vol.1)E, p. xviii + 327 pp.

Transport Canada. 2019. Protecting North Atlantic right whales from collisions with ships in the Gulf of St. Lawrence. Available from http://www.tc.gc.ca/en/services/marine/navigation-marine-conditions/protecting-north-atlantic-right-whales-collisions-ships-gulf-st-lawrence.html [accessed 2019-05-23 2019].

Trygonis, V., Gerstein, E., Moir, J., and McCulloch, S. 2013. Vocalization characteristics of North Atlantic right whale surface active groups in the calving habitat, southeastern United States. J. Acoust. Soc. Am. **134**(6): 4518-4531.

Urazghildiiev, I.R., and Clark, C.W. 2007. Acoustic detection of North Atlantic right whale contact calls using spectrogram-based statistics. J. Acoust. Soc. Am. **122**(2): 769-776.

Urazghildiiev, I.R., Clark, C.W., and Krein, T.P. 2009. Detection and recognition of North Atlantic right whale contact calls in the presence of ambient noise. IEEE J Ocean Eng **34**(3): 358-368.

Wenz, G.M. 1962. Acoustic ambient noise in the ocean: Spectra and sources. J. Acoust. Soc. Am. **34**(12): 1936-1956.

Wiggins, S.M., McDonald, M.A., Munger, L.M., Moore, S.E., and Hildebrand, J.A. 2004. Waveguide propagation allows range estimates for north pacific right whales in the bering sea. Can. Acoust. **32**(2): 146-154.

ANNEX 1: OPTIMAL FFT WINDOW LENGTH FOR NARW UPCALL

Here, we demonstrate that an optimal length for the window used to compute the spectrogram exists in order to maximize the processing gain (ratio of the SNR after the computation of the STFT (short-time Fourier transform) with the SNR of the raw data). The demonstration is run for 2 types of signal. The first one is a cosine of duration T and the optimal length is T. The second one is a LFM (NARW upcall like) and the optimal length depends on the modulation rate.

Processing Gain estimation from the spectrogram of monochromatic non-modulated sounds

Our measure is the sum of 1) a monochromatic, non-modulated signal of amplitude A and a duration of M samples centered around time t(o) and a frequency f_0 (with $f_0 = f(p) = pF_e/L$), and 2) of a Gaussian stationary white noise with mean $\mu = 0$ and variance σ^2.
The measure is defined by:

$$n \in [0, N-1]$$
$$m(nTe) = A\exp(2\pi j f_0 nTe) + b(n) \quad \forall n \in [o - M/2 + 1, o + M/2]$$
$$m(nTe) = 0 + b(n) \quad elsewhere$$

where T_e is the sampling period, and b(n) is a Gaussian stationary white noise.

The SNR of the raw measurements, SNR_{be}, is defined as follows:

$$SNR_{be} = \frac{A^2}{\sigma^2}$$

We compute the STFT of the signal in [t(o),f(p)] with a rectangular window of length L. The analytical computations of the STFT and the spectrogram in the case of target signal-only data, as well as the analytical computations of the STFT and the mean value of the spectrogram of noise-only data are not referred here. The estimation of the SNR_{af} after calculating the STFT at the segment [t(o),f(p)] can be obtained through:

$$\frac{SNR_{af}}{SNR_{be}} = GT = M \times \frac{L}{M} = L; \ \forall L < M$$
$$\frac{SNR_{af}}{SNR_{be}} = GT = M \times \frac{M}{L} = \frac{M^2}{L}; \ \forall L \geq M$$

Figure 26 (box 1) reveals that the processing gain (PG) reaches a maximum when the length of the window L equals the length of the monochromatic signal. This phenomenon is further outlined in figure 27 using real data. The recordings were made in presence of belugas

(*Delphinapterus leucas*) in the St. Lawrence Estuary, Canada, at a depth of 5 m and with a sampling frequency of 16384 sa/s. The temporal representation of the measure (Figure 27, A) does not enable the detection of the vocalizations. This is not the case of the spectrogram representation, in which the sounds are clearly visible (Figure 27, panel B) as monochromatic signals (constant frequency) of 1-s duration. One second corresponds to an optimal length L of 16384 samples. This is emphasized when comparing the spectrograms of panels C, computed using L = 2048 and D calculated using L = 16384. The whistles are better evidenced in panel D than in panel C and have therefore a better SNR.

Processing Gain estimation from the spectrogram of linear, frequency-modulated sounds

We address the case of linear frequency-modulated sounds (NARW upcall like, Figure 26, box 2).

In this case, the data are defined by:

$$n \in [0, N-1]$$
$$m(nT_e) = s_u(nT_e) + b(n) \quad \forall n \in [o - M/2 + 1, o + M/2]$$
$$m(nT_e) = 0 + b(n) \; elsewhere$$
$$s_u(nT_e) = A\exp(2\pi j f_0 nT_e + 2\pi \frac{\alpha}{2}(nT_e)^2)$$

The artificial signal is the sum of a linear frequency-modulation of amplitude A, with a duration of M samples centered around time t(o) and a center frequency f_0 (with $f_0 = f(p) = pF_e/L$) as well as a modulation rate (slope) α (Hz/s), and of a Gaussian stationary white noise with $\mu = 0$ and a variance σ^2.

We suppose that the STFT of the signal in [t(o),f(p)] is calculated with a rectangular window of length L. The analytical computations of the STFT and the spectrogram in the case of a target signal-only data as well as the analytical computations of the STFT and the mean value of the spectrogram of noise-only data are not referred here. The estimation of the SNR_{af} after STFT computing the FFT of the segment [t(o),f(p)] can be assessed from:

$$\frac{SNR_{af}}{SNR_{be}} = GT = \frac{L_0^2}{L}\left|C(\frac{L}{L_0}) + jS(\frac{L}{L_0})\right|^2$$

$$L_0\,(sample) = \sqrt{\frac{2}{\alpha}}\,f_e$$

$$T_0\,(second) = \sqrt{\frac{2}{\alpha}}$$

$$PG_{\max} = PG(L_0) = 0.8L_0$$

where C et S are the Bessel integrals in sine and cosine (Abramowitz and Stegun 1974)

Figure 26 (box 2) reveals that the processing gain (PG) reaches a maximum when the length of the window L equals L_0. This phenomenon is further outlined in Figure 28 using real data. The recordings were made in presence of bottlenose dolphins (*Tursiops truncatus*) in the Iroise Sea, Brest, France at a depth of 5 m and with a sampling frequency of 44000 sa/s. Plot A of Figure 28 shows the temporal representation of the recordings using a bandpass filter starting at 2000 Hz. In the spectrogram representation (Figure 28, plot B), three whistles are clearly visible, all with an almost linear frequency-modulated portion of 0.5 s duration and a frequency band of almost 10 kHz. The modulation rate therefore corresponds to 20000 Hz/s with an optimal STFT length of 512 points. This is emphasized when comparing the spectrograms computed using different window sizes L. Figure 28 illustrates three examples: spectrogram C, computed with a window length L = 128, spectrogram D with L = 512, and spectrogram E with L = 16384. The whistles are better evidenced in panel D compared to the two other panels. The window length that maximizes the SNR of the modulated signal corresponds to the one resulting in a better time-frequency resolution of the STFT. Optimizing the SNR therefore means to concentrate the energy along the modulated portion of the signal (e.g. narrower and higher peaks in panel D than in panel E).

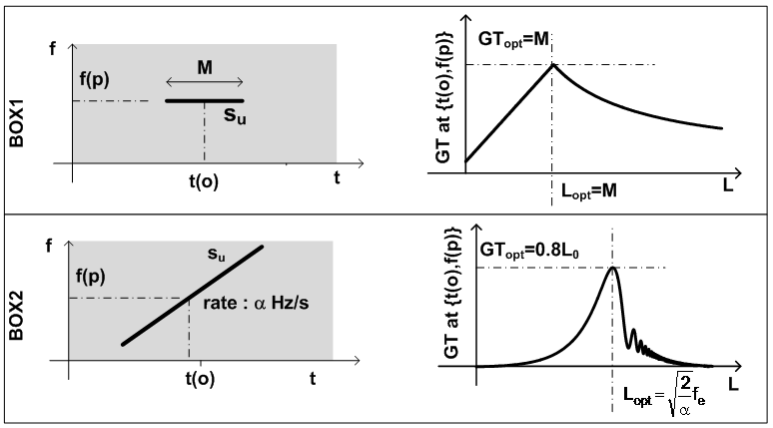

Figure 26. Theoretical SNR and processing gain (PG) of the STFT as a function of the window length L.
BOX1: non-modulated monochromatic pulses; BOX2: signals with linear frequency modulation.

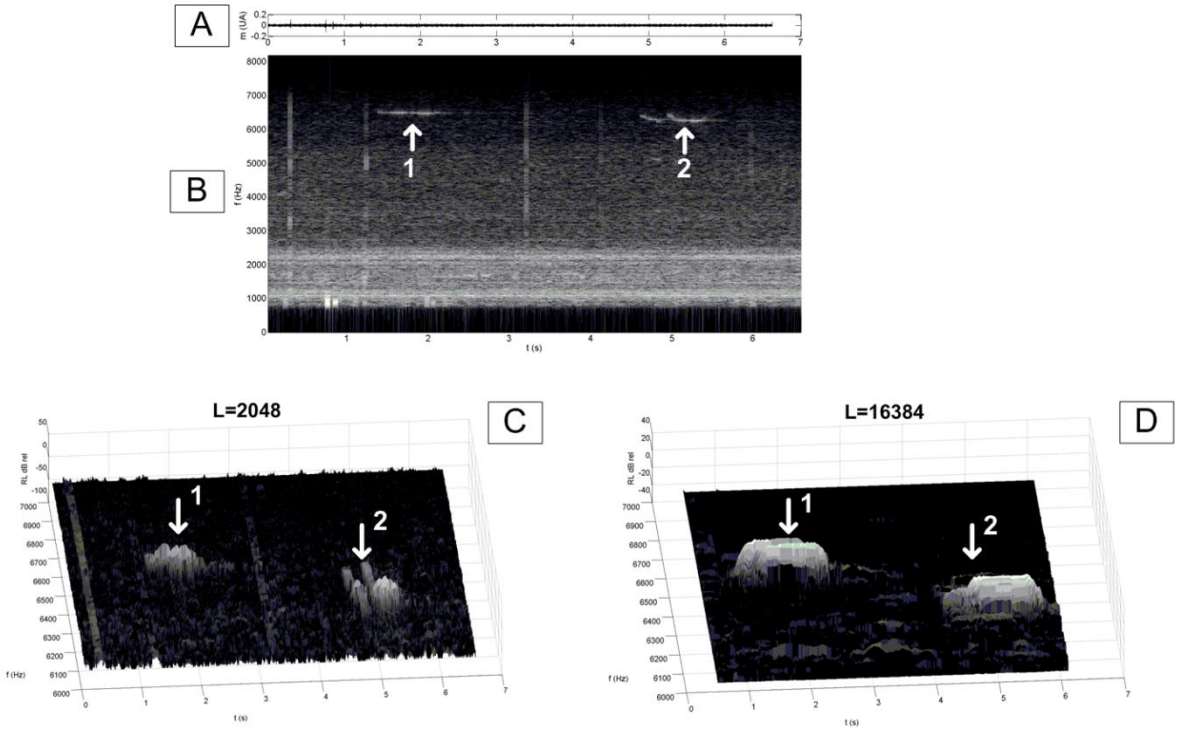

Figure 27. Application of the STFT real recordings containing two whistles of beluga whales (*Delphinapterus leucas*) with constant frequency.
A: raw data, B: 2D spectrogram with optimal length of the FFT window, C: 3D spectrogram with a smaller length of FFT window lower than the optimal one shown at panel D.

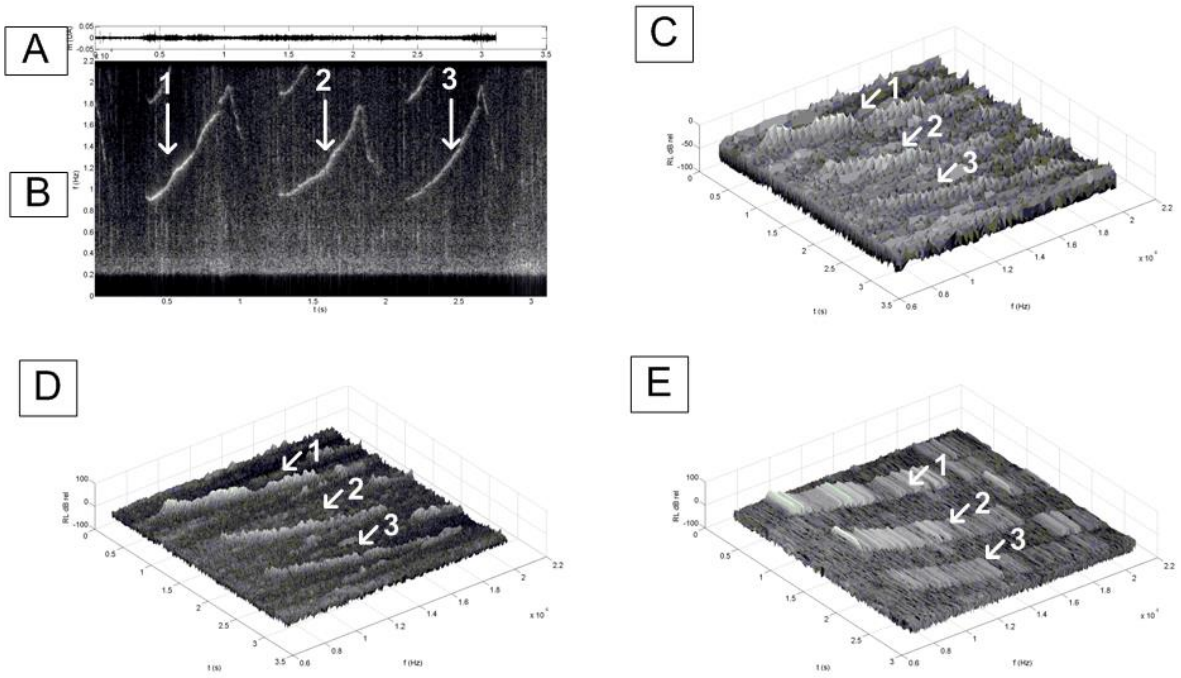

Figure 28. Application of the STFT on real recordings containing three whistles of bottlenose dolphins (*Tursiops truncatus*) with a portion of the sound representing a linear frequency-modulated signal.
A: raw data, B: 2D spectrogram with optimal length of FFT window, C) 3D spectrogram with a smaller window than the optimal one, D) 3D spectrogram with optimal length of FFT window, E) 3D spectrogram with larger window than the optimal one.

ANNEX 2: DETAILS OF ROC CURVES OF THE UPCALL DETECTOR

Here we detail the computation of the ROC of TFBD shown in Table 5. Let the measurements according to the model be:

Hypothesis H_0: $m(t) = b_{tot}(t)$

Hypothesis H_1: $m(t) = uc(t) + b_{tot}(t)$

$b_{tot}(t)$ is the noise and uc(t) is the upcall. $b_{tot}(t)$ is assumed to be random and normally distributed (0 mean, variance σ^2), whereas uc(t) is a deterministic signal:
$uc(t) = 0\ if\ t \notin [0,T], uc(t) = A\cos(2\pi f_{min} t + 2\pi \frac{f_{max}-f_{min}}{2T} t^2)$.

TFBD implies three stages of processing shown in Figure 29:

- Step 1: Computation of the spectrogram,
- Step 2: Binarization at the scale of the pixel of the spectrogram,
- Step 3: Evaluation of the number of time-frequency bins coinciding with those inside the time-frequency template of the upcall
- Final decision: test this number against a detection threshold for upcall presence.

Steps 1 and 2 follow the development of Dadouchi et al. (2013). Let L_{fft} be the length (in samples) of the FFT used to compute the spectrogram (chosen to be optimal as in annex 1) and $P_{fa\ pix}$ and $P_{d\ pix}$ the probability of false alarm and detection at the scale of the pixel after stage 2.

Under the hypothesis H0 (noise only), the spectrogram is a random variable and follows a centralized chi^2 law with 2 degrees of freedom (mean $L_{fft}\sigma^2$, standard deviation $L_{fft}\sigma^2$).

Under the hypothesis H1 (noise and upcall), the spectrogram is a random variable and follows a shifted non-centered chi^2 law with 2 degrees of freedom (mean $A^2/2L_{fft}^2+L_{fft}\sigma^2$, standard deviation $L_{fft}\sigma^2$).

Without changing the values of $P_{fa\ pix}$ and $P_{d\ pix}$, we can scale the argument of the law by $L_{fft}\sigma^2$, then we have:

- Under the hypothesis H0 (noise only), the spectrogram is a random variable and follows a centralized chi^2 law with 2 degrees of freedom (mean 1, standard deviation 1).
- Under the hypothesis H1 (noise and upcall), the spectrogram is a random variable and follows a non-centered chi^2 law with 2 degrees of freedom (mean $1 + 0.8\frac{A^2}{2}\frac{L_{fft}}{\sigma^2}$, standard deviation 1).

The factor $\frac{A^2}{2}\frac{L_{fft}}{\sigma^2}$ is equal to $\frac{A^2}{2}\frac{L_{fft}}{\gamma_0 \times f_s} = \frac{A^2}{2}\frac{T_{fft}}{\gamma_0}$, where T_{fft} is the length of the FFT windows in second and γ_0 is the power spectrum of the ambient noise ($\mu Pa^2/Hz$).

Then we have:

$$P_{d\,pix} = 1 - ncX2cdf\left(-2\log\left(P_{fa\,pix}\right), 2, 0.8\frac{A^2 T_{fft}}{2\gamma_0}\right),$$

with:

ncX2cdf(x,p,q): cumulative distribution function computed at x of a non-central chi^2 law with p degrees of freedom and a parameter of non-centrality equal to q

chi^{2}inv(x,p): reciprocal function computed at x of the cumulative distribution function of the centralized chi^2 law with p degrees of freedom.

At the end of step 2, we have a discrete spectrogram and step 3 processes it by looking for the instants where an upcall is present by counting the number of pixels equal to 1 in a time-frequency template of the upcall; this number is tested to decide if an upcall is present. Let P be the number of time-frequency pixels needed to cover the time-frequency template of the upcall; we can calculate the probability to have j pixels equal to 1 into the P possible pixels. This is the probability to obtain j draws equal to 1 among P draws knowing that the probability to obtain 1 for 1 draw is $P_{d\,pix}$ under hypotheses H_1 and $P_{fa\,pix}$ under hypotheses H_0.

Considering that time-frequency pixels are independent in first approximation, the number i follows a binomial law:

$$f_Q(j, H_0) = \binom{P}{j} (P_{fa\,pix})^j (1 - P_{fa\,pix})^{P-j}$$
$$f_Q(j, H_1) = \binom{P}{j} (P_{d\,pix})^j (1 - P_{d\,pix})^{P-j}$$

The presence of an upcall (decision D1) is decided if the number of draws among P is more than a threshold λ_2, while the absence of an upcall (decision D0) is decided if the number of draws among P is less than a threshold λ_2 ; then we have:

$$\boldsymbol{P_{fa}} = 1 - F_Q(\lambda_2, H_0)$$
$$\boldsymbol{P_d} = 1 - F_Q(\lambda_2, H_1)$$
$$F_Q(\lambda_2, H_0) = \sum_{j=0}^{\lambda_2} \binom{P}{j} (P_{fa\,pix})^j (1 - P_{fa\,pix})^{P-j}$$
$$F_Q(\lambda_2, H_1) = \sum_{j=0}^{\lambda_2} \binom{P}{j} (P_{d\,pix})^j (1 - P_{d\,pix})^{P-j}.$$

To evaluate the ROC of TFBD, one must follow the steps:

- set $p_{fa\,pix} = 10^{-3}$, $p_{fa} = 2 \times 10^{-6}$
- from $P_{fa} = 1 - F_Q(\lambda_2, H_0)$ find λ_2
- from $P_{d\,pix} = 1 - ncX2cdf\left(-2\log\left(P_{fa\,pix}\right), 2, 0.8\frac{A^2 T_{fft}}{2\gamma_0}\right)$ find $P_{d\,pix}$
- from $P_d = 1 - F_Q(\lambda_2, H_1)$ find P_d.

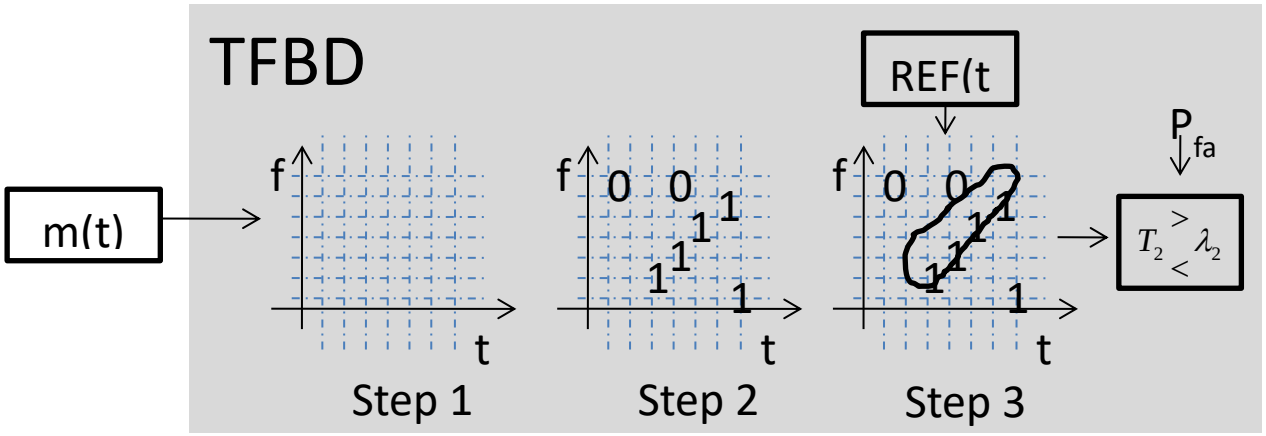

Figure 29. TFBD processing chain.

Step 1 computes the spectrogram of the data, step 2 binarizes the spectrogram at the scale of 1 pixel, step 3 works at the scale of 1 time-frequency region and looks for areas where the upcall is present by counting the number of pixels equal to 1 in a time-frequency template of the upcall; this number is tested to decide if an upcall is present.

ANNEX 3: EFFECT ON THE PROCESSING GAIN OF A MISFIT BETWEEN THE REFERENCE AND THE TRUE SIGNAL FOR CCBD

Here we examine how the processing gain of CCBD decreases with the level of misfit between the measurement and the upcall reference used for the cross-correlation. We simulate a measurement made with noise plus a LFM upcall with features (T_0, $f_{min,0}$, $f_{max,0}$) called LFM_0. As optimal processing, the measurement is cross-correlated with LFM_0, the maximum of the correlation Γ_0 is noted. Then we simulate a sub-optimal reference as a LFM with features (T, f_{min}, f_{max}) and the measurement is cross-correlated with LFM, then the maximum of the correlation Γ is noted. As LFM is different from LFM_0, $\Gamma < \Gamma_0$, we define the loss of processing gain as:

$$\Delta PG = 10log_{10}(\frac{\Gamma}{\Gamma_0}).$$

To assess the level processing gain loss as a function of the level of misfit between the true and the used references, we define a percentage of deviation of the features (T, f_{min}, f_{max}) vs (T_0, $f_{min,0}$, $f_{max,0}$) and we choose a number N_{MC} of Monte Carlo simulations. For each Monte Carlo simulation, we randomly draw the value of (T, f_{min}, f_{max}), we cross-correlate the measurement with LFM(T, f_{min}, f_{max}), and we evaluate Γ and ΔPG. We keep in memory each ΔPG for each MC simulation. At the end of the N_{MC} Monte Carlo simulations, we evaluate the mean ($\overline{\Delta PG}$) and the standard deviation $\sigma\Delta PG$ of ΔPG.

Figure 30 presents $\overline{\Delta PG}$ and $\sigma\Delta PG$ for N_{MC} = 1000 and the percentage of misfit from 0% to 50%. From 10% of misfit between the features of the LFM, the average loss of processing gain is at least 4 dB.

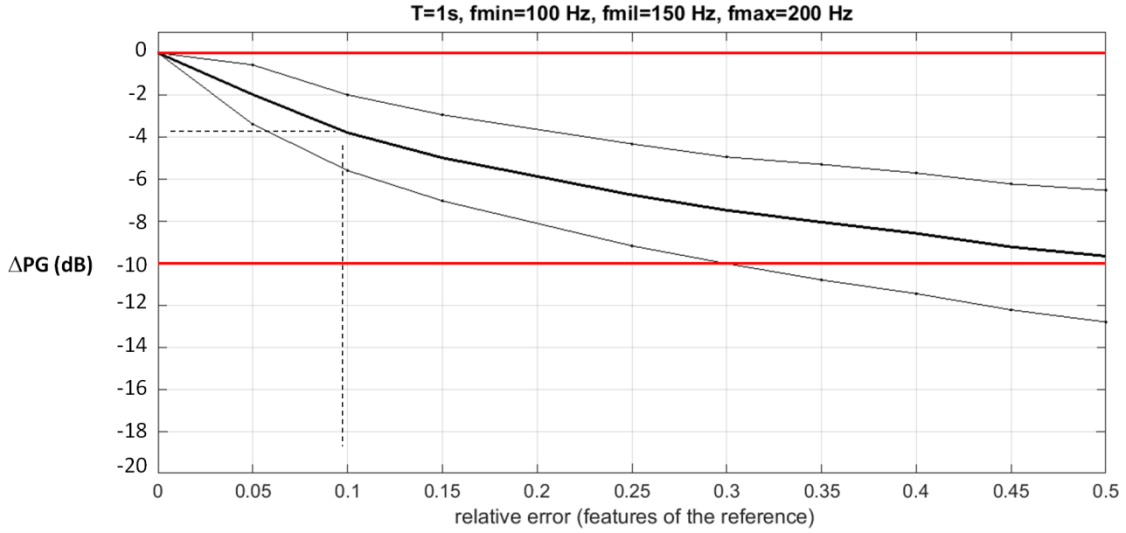

Figure 30. Loss in processing gain as a function of the level of misfit between the true and the used references, thick black curve $\overline{\Delta PG}$, thin black curves: $\overline{\Delta PG} \pm \sigma\Delta PG$.